الجـمـهوريــة الجــز ائريــة الـديمقــراطيـة الـشـعبيــة
People's Democratic Republic of Algeria
وزارة الـتـعـليــم الـعــالي و الـبحـث الـعـلــمي
Ministery of Higher Education and Scientific Research
جــامعــة عبد الحميــد بن باديــس – مستغانــم
Abdel Hamid Ibn Badis University – Mostaganem
كـليــة الـعلــوم و الـتكنـولـوجــيـا
Faculty of Sciences and Technology
قـسم الهـنـدســة الميكانيكية

Department of Mechanical Engineering

N° d'ordre : M2....../GM/2024

MASTER'S DEGREE THESIS

Field of study: Mechanical Engineering
Specialization: Mechanical Construction

Thème

Study of the Vibration Behavior of FGM Porous Plates Based on Trigonometry

Presented by:

1-KAIM Yahia

Defended on June 28, 2026, before the Examination Committee composed of:

Chairperson:	Dr. BENKHATTAB Mohamed	Maitre de Conférences "A"	UMAB
Examiner:	Dr. BENKABOUCHE Saleh Eddine	Maitre de Conférences "B"	UMAB
Supervisor :	Dr. HEBBAR Imène	Maitre de Conférences "B"	UMAB

Academic Year: 2025/2026

Acknowledgments

First and foremost, I would like to thank Almighty Allah for granting me health, strength, determination, and patience to accomplish this modest work. His guidance and blessings have been my greatest source of support throughout this journey.

I extend my deepest and most heartfelt gratitude to my beloved parents. Their unwavering support, endless sacrifices, unconditional love, and constant encouragement have been the foundation of my success. Words cannot fully express my profound appreciation and everlasting love for them.

I would like to express my sincere and heartfelt gratitude to my supervisor, **Dr. I. HEBBAR**, for her invaluable guidance, continuous support, availability, and scientific rigor throughout this research. Her insightful advice and constructive suggestions have greatly contributed to the quality and completion of this work. I am deeply grateful for her dedication and wish her continued success, happiness, and blessings in both her professional and personal life.

I would also like to express my sincere appreciation to **Dr. BENKABOUCHE** and **Dr. BENKHETTAB** for the interest they have shown in this work by kindly accepting to serve as members of the examination committee. Their time and valuable evaluation are greatly appreciated.

Finally, I would like to thank all my teachers for sharing their knowledge and expertise throughout my academic journey. I also extend my gratitude to the entire administrative staff for their kindness, professionalism, and support.

List of Figures

List of Tables

List of Symbols and Notations

a, b	Plate length and width
h	Total plate thickness
x, y, z	Cartesian coordinates (z is through-thickness, origin at mid-plane)
p	Power-law index (volume fraction exponent)
E	Porosity volume fraction
E(z)	Young's modulus as a function of z
Ec, Em	Young's modulus of ceramic and metal
P(z)	Mass density as a function of z
Pc, ρm	Mass density of ceramic and metal
N	Poisson's ratio (assumed constant)
u_0,v_0	Mid-plane in-plane displacements (in x and y directions)
w_0	Transverse displacement (deflection)
θ	Additional rotation variable associated with transverse shear
f(z)	Sinusoidal shape function, $f(z) = (h/\pi) \sin(\pi z/h)$
Q_{ij}	Elastic stiffness coefficients (i,j = 1,2,6,4,5)
A_{ij}, B_{ij}, D_{ij}	Extensional, coupling, and bending stiffnesses
B_{ij}^s, D_{ij}^s, H_{ij}^s	Higher-order coupling and bending stiffnesses (associated with f(z))
A_{ij}^s	Transverse shear stiffnesses
I_1, I_2, I_3, I_4, I_5 ,I_6	Mass inertias
N_i, M_i , S_i	Stress resultants : membrane (N), bending moment (M), higher-order moment (S) (i = x,y,xy)
N_{xz}, N_{yz}	Generalized transverse shear forces
ω	Natural circular frequency (angular frequency)
$\hat{\omega}$	Dimensionless frequency : $\omega h\sqrt{(\rho_c/E_c)}$
$\bar{\omega}$	Dimensionless frequency : $\omega (a^2/h) \sqrt{(\rho_c/E_c)}$
α, β	Wave numbers : $\alpha = m\pi/a$, $\beta = n\pi/b$
m, n	Mode numbers (half-waves in x and y directions)
t	Time
U, K	Strain energy and kinetic energy
δ	Variational operator
[K], [M]	Stiffness and mass matrices
Δ	Vector of modal amplitudes $\{U_{mn},V_{mn},W_{mn},\Theta_{mn}\}^T$
σ_x, σ_y , τ_{xy}, τ_{xz} τ_{yz}	Stresses (normal and shear)
ε_x, ε_y, γ_{xy}, γ_{xz}, γ_{yz}	Strains (normal and shear)

الملخص

تتناول هذه المذكرة التحليل الديناميكي للصفائح المصنوعة من المواد متدرجة الخواص (FGM) باستخدام نظرية مثلثية لتشوه القص. وتتميز المواد متدرجة الخواص (FGM) بتدرج مستمر في خصائصها الميكانيكية عبر السمك، مما يساهم في تحسين أدائها البنيوي والميكانيكي بشكل عام.

ولإبراز التأثيرات المعقدة لتوزيع المسامية، تم افتراض أن خواص المادة تتغير وفق قانون أسّي معدل يأخذ في الاعتبار أربعة أنماط مختلفة لتوزيع المسامية، وذلك بدلالة مؤشر تدرج المادة (p) ومؤشر المسامية.

أُجريت دراسة بارامترية لتحليل تأثير عدة عوامل، من بينها مؤشر تدرج المادة(p) ، والنسبة الهندسية (a/h)، ونوع توزيع المسامية، على الترددات الطبيعية اللابعدية للصفائح المسامية المصنوعة من المواد متدرجة الخواص.

وأظهرت النتائج العددية توافقًا جيدًا مع النتائج المنشورة في الأدبيات العلمية، مما يؤكد صحة النموذج المقترح ودقته.

الكلمات المفتاحية :صفائح المواد متدرجة الخواص(FGM) ، نظرية تشوه القص من الرتبة العليا (HSDT)، الاهتزازات الحرة، المسامية.

Abstract

This thesis deals with the dynamic analysis of functionally graded material (FGM) plates using a trigonometric shear deformation theory. FGM materials are characterized by a gradual variation of their mechanical properties through the thickness, which improves their overall structural performance.

To highlight the complex effects of porosity distribution, the material properties are assumed to vary according to a modified power-law distribution that takes into account four different porosity distributions as a function of the material index (p) and the porosity index.

A parametric study was carried out to investigate the influence of several parameters, including the material index (p), the geometric ratio (a/h), and the type of porosity distribution on the dimensionless natural frequencies of porous FGM plates.

The numerical results obtained are in good agreement with those reported in the literature, confirming the validity and accuracy of the proposed model.

Keywords: FGM plates, higher-order shear deformation theory (HSDT), free vibration, porosity.

Résumé

Ce mémoire porte sur l'analyse dynamique des plaques en matériaux à gradient fonctionnel (FGM) en utilisant une théorie trigonométrique de déformation en cisaillement. Les matériaux à gradient fonctionnel (FGM) se caractérisent par une variation continue de leurs propriétés mécaniques à travers l'épaisseur, ce qui permet d'améliorer leurs performances structurelles globales.

Afin de mettre en évidence les effets complexes de la distribution de la porosité, les propriétés du matériau sont supposées varier suivant une loi de puissance modifiée prenant en compte quatre distributions différentes de la porosité, en fonction de l'indice de gradient du matériau (p) et de l'indice de porosité.

Une étude paramétrique a été réalisée afin d'examiner l'influence de plusieurs paramètres, notamment l'indice de gradient (p), le rapport géométrique (a/h) ainsi que le type de distribution de la porosité, sur les fréquences propres adimensionnelles des plaques FGM poreuses.Les résultats numériques obtenus sont en bon accord avec ceux rapportés dans la littérature, ce qui confirme la validité et la précision du modèle proposé.

Mots-clés : plaques FGM, théorie de déformation en cisaillement d'ordre supérieur (HSDT), vibrations libres, porosité.

Table des matières

General Introduction

In recent years, the industrial world has experienced remarkable evolution due to advances in science. Intensive scientific research has been carried out to design innovative processes and high-performance materials meeting the incessant needs of industry.

Functionally Graded Materials (FGMs) have strongly proven their presence in the industrial world and have gained great popularity due to their considerable thermal and mechanical capabilities. These materials are a new generation of composite materials, first introduced by a Japanese scientific group in 1984 [22, 23].

FGMs are obtained by continuously varying the constituents of multi-phase materials within a predetermined volume fraction of the constitutive material. The power-law function and the exponential function are employed to describe the variations of material properties of FGMs, with the appearance of stress concentrations at the interfaces where the material is continuous but changes gradually.

A number of works dealing with various aspects of FGMs have been published in recent decades. They show that most of the early research on FGMs focused on the analysis of mechanical behavior and fracture treatment under the effect of mechanical loading and thermal stresses, based on finite element calculations.

The modeling of FGM plates has been the subject of numerous research works using different plate theories. The Classical Plate Theory (CPT), developed by Kirchhoff [1], neglects transverse shear effects and remains valid only for thin plates. To improve this approach, Mindlin [2] proposed the First-order Shear Deformation Theory (FSDT), which accounts for transverse shear effects but requires the use of a shear correction factor. Subsequently, several refined Higher-order Shear Deformation Theories (HSDT) have been developed to obtain a more realistic description of thick plate behavior without resorting to correction factors [3–6].

The main objective of this thesis work is to analyze the influence of porosity distribution on the free vibration behavior of porous FGM plates, based on advanced theoretical modeling and accurate analytical solutions.

The outline of this thesis is organized into four chapters as follows:

Chapter 1 is devoted to FGM materials, their uses, developments, and fields of application. The different laws governing the variation of their properties are also presented.

Chapter 2 is dedicated to a review of the different plate theories used in the analysis of FGM structures.

Chapter 3 is devoted to the mathematical formulation and the higher-order shear deformation theory (HSDT) model adopted for the study of porous plates.

Chapter 4 is reserved for the obtained numerical results, their interpretation, as well as a detailed discussion of the influence of the various studied parameters.

Chapitre I :

General Information on FGM Materials

1.1 Introduction

The development of composite materials has enabled the integration of distinct, specialized properties within a single structural component. However, achieving localized optimization—such as bonding a high-hardness material to the surface of a tough substrate—frequently introduces severe interfacial challenges. This abrupt compositional transition can induce significant localized stress concentrations.

To mitigate this singularity, Functionally Graded Materials (FGMs) offer an elegant solution by implementing a continuous spatial transition of the desired properties via a composition gradient. Characterized as an advanced class of composites, FGMs feature a seamless, uninterrupted variation of constituent volume fractions, typically through the thickness direction, to achieve a well-defined property profile. Consequently, this type of material has garnered substantial research attention recently due to its exceptional capability to suppress material property mismatches and drastically reduce thermal stresses.

1.2 General Overview of FGM Development

In 1987, the Japanese government launched a comprehensive research project entitled "Research on the Basic Technology for the Development of Functionally Graded Materials and the Study of Thermal Stress Relaxation". The primary objective of this project was to develop materials featuring structural configurations capable of serving as thermal barriers for aerospace programs. The materials constituting spacecraft walls are required to operate at surface temperatures reaching 1800°C, under temperature gradients of approximately 1300°C. At that time, no existing industrial material was capable of enduring such severe thermomechanical loads. Consequently, three key characteristics must be considered for the design of these materials:

- High-temperature thermal and oxidation resistance at the material's surface layer;
- High material toughness on the lower-temperature side;
- Effective thermal stress relaxation throughout the material profile.

1.3 Concept of Functionally Graded Materials (FGMs)

Functionally Graded Materials are distinguished from traditional composite materials by the gradual and continuous variation of their mechanical and thermal properties across the thickness profile, governed by a specific functional law. This continuous transition prevents stress concentrations at the interfaces—which typically cause delamination—while enhancing the overall mechanical and thermal performance of the component through the strategic combination of constituent materials.

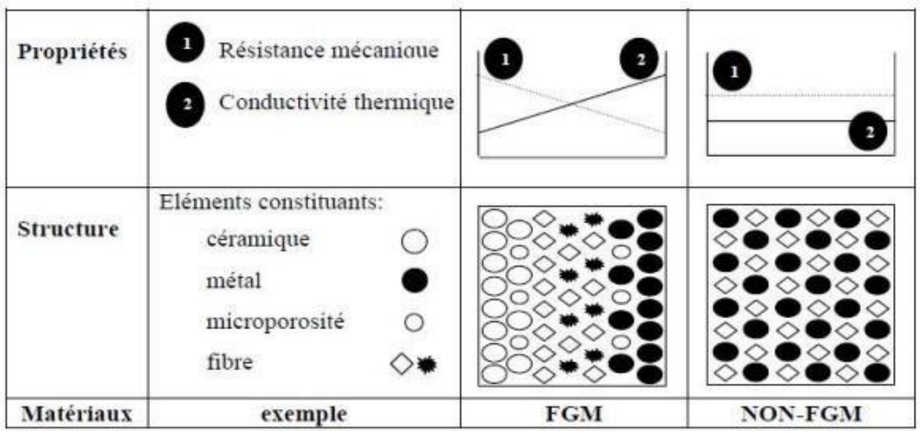

Figure 1.1. Comparison between traditional composite materials and FGM [23]

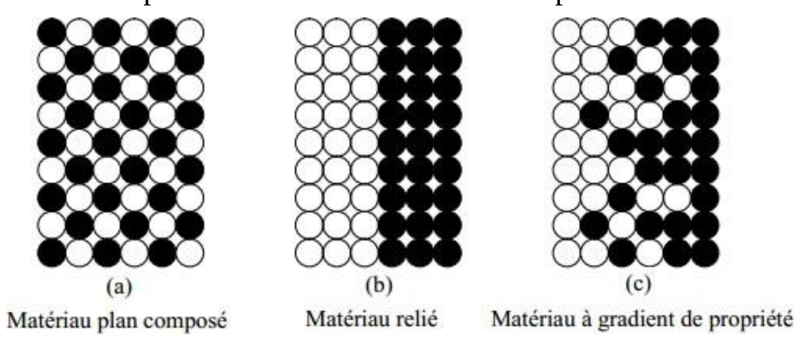

Figure 1.2. Difference in distribution [22]

Classification based on Phase Morphology and Structural Scale

- Chemical Composition Gradient The chemical composition and elemental distribution are systematically varied as a function of spatial coordinates within the material volume to tailor localized macroscopic properties.
- Porosity Gradient (Porously Graded FGMs) The void fraction or porosity density varies continuously along specific geometric coordinates. In these architectures, both the spatial pore size distribution and the geometric pore morphology (shape and orientation) are critical factors dictating the effective mechanical response.

• Microstructural Gradient The material exhibits distinct microstructural phases or grain configurations between its surface layer and its core matrix. This structural variation is primarily governed by local cooling rate differentials during solidification, where subsequent post-processing heat treatments play a pivotal role in phase stabilization [5].

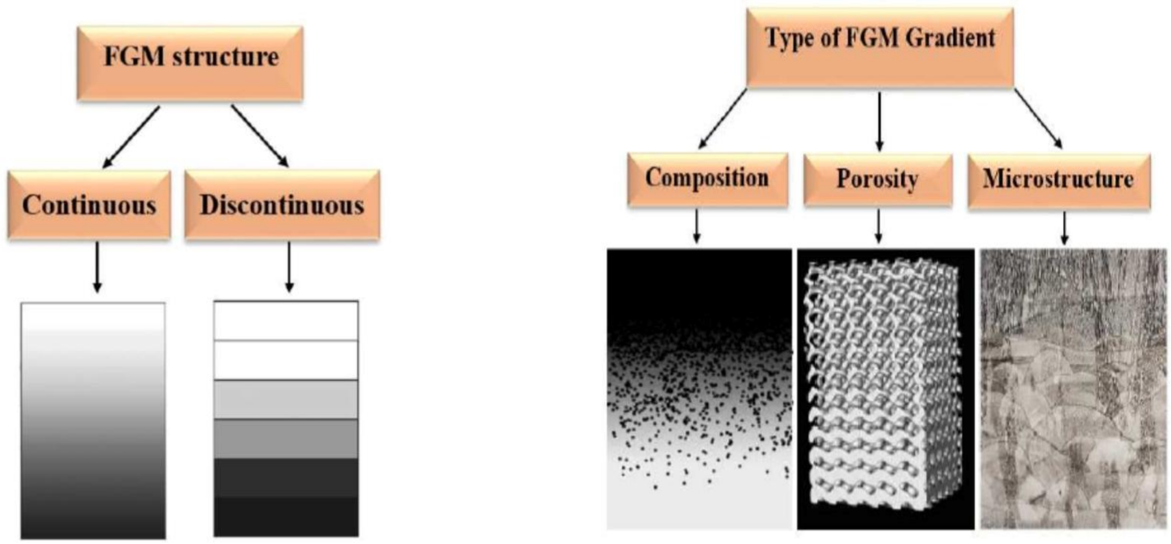

Figure 1.3. An example of functionally graded materials (FGMs) that can be analyzed using plate theories [5].

1.4 Porosity Phenomenon in FGM Plates

Within Functionally Graded Materials (FGMs), porosity is a prevalent phenomenon that frequently originates during processing operations [6]. A prominent example is the Centrifugal Mixing Powder Method (CMPM), which involves introducing a baseline mixture of matrix powder (metal) and reinforcement powder (ceramic) into a rotating mold, followed by the infiltration of molten metal to fill the inter-particle voids under the influence of centrifugal forces [10]. Pores typically develop due to disparities in the solidification rates and thermal contraction coefficients of the constituent phases, ultimately inducing micro-void entrapment within the final structural matrix [6].

The inclusion of such voids substantially alters the macroscopic mechanical performance of FGM plates [6]. While the explicit influence of these microstructural imperfections on the dynamic response and vibrational behavior will be thoroughly analyzed in subsequent sections, it is fundamentally established that porosity induces a concurrent reduction in both the effective structural stiffness and the overall mass density. However, prior to implementing the structural model, it is essential to systematically categorize the distinct spatial topologies and geometric distribution profiles of porosity across FGM plate configurations.

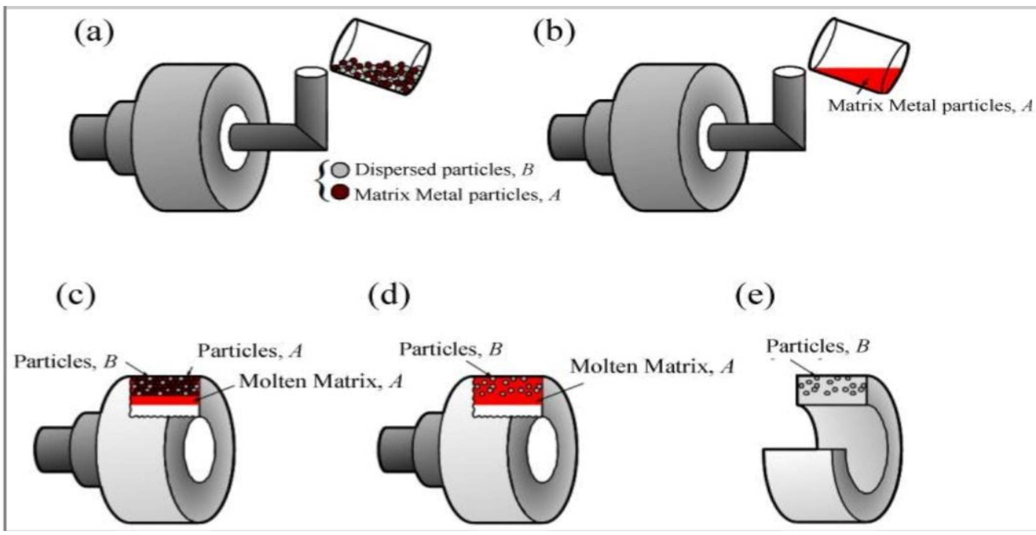

Figure 1.4. The schematic description of CSPM [10].

1.5 Types of Porosity Distribution

Porosity distribution patterns in FGM plates vary and typically include the following:

1.5.1 Uniform Porosity

Where the pores are distributed uniformly throughout the plate thickness.

1.5.2 Non-uniform Porosity

Where the distribution of pores across the thickness of the plate is random. It can be

- Non-uniform symmetric

- Non-uniform asymmetric [11].

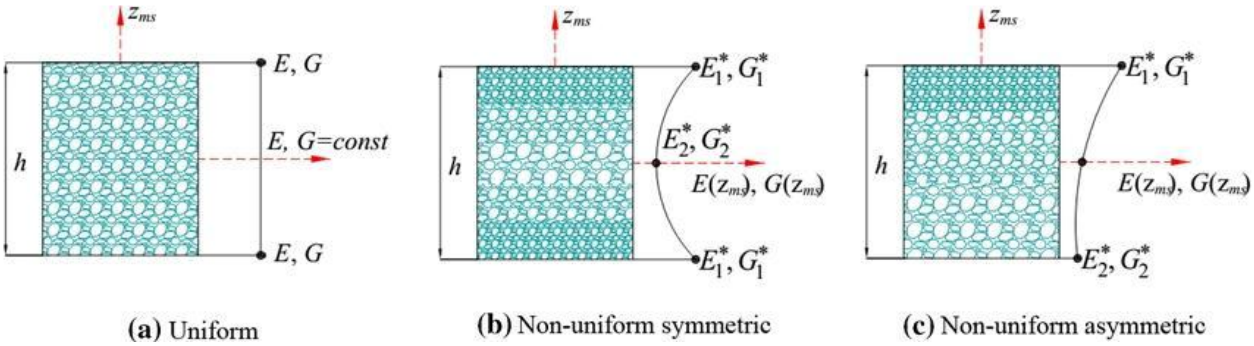

Figure 1.5.Types of Porosity Distribution [11].

1.6 Porosity Distribution Patterns

The non-uniform porosity exhibits the following distribution patterns:

O-Type, The pores are concentrated in an O-shape at the center of the plate.

X-Type, The pores are arranged in an hourglass shape, making them resemble the letter X.

V-Type, The pores increase gradually from the bottom surface to the top, making them resemble the letter V[8].

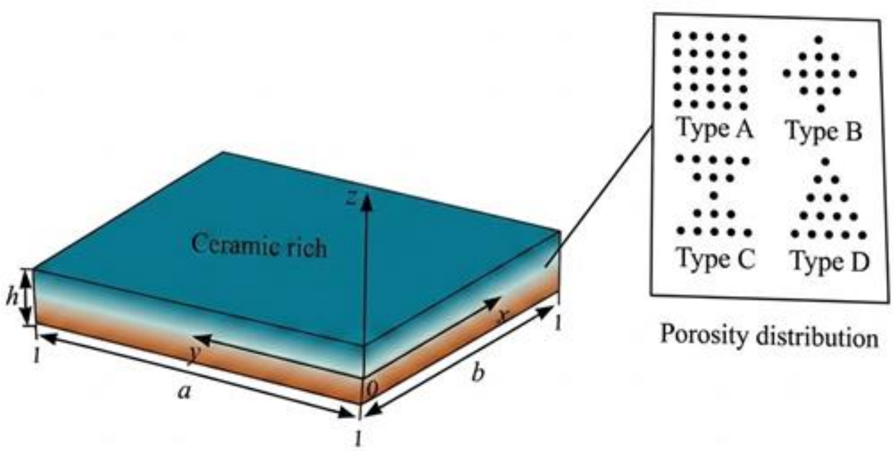

Figure 1.6. Illustrates the pore structures in the FGM plate for metals and ceramics [8]

It should be noted that these idealized geometric shapes and distribution patterns provide approximate macroscopic representations, as actual experimental porosities rarely conform to strict mathematical profiles. Consequently, these deterministic distributions remain hypothetical frameworks designed to approximate real-world microstructures [7] when explicit porosity mapping is unavailable. This naturally raises the critical question of how these internal voids can be characterized. To address this, several non-destructive evaluation techniques are utilized to detect porosity within FGMs, as identifying void topologies and understanding their spatial distribution is paramount for assessing the structural integrity and mechanical performance of FGM plates.

1.7 Scanning Electron Microscopy (SEM)

SEM is a powerful and effective tool that provides high-resolution images of the microstructure of materials and identifies pores by their size, shape, and distribution. It also provides details on the shape, size, and orientation of fine grains, as well as on plate-like particles such as Al_3Ti compounds, in addition to detecting microscopic defects such as pores and voids [49,10].

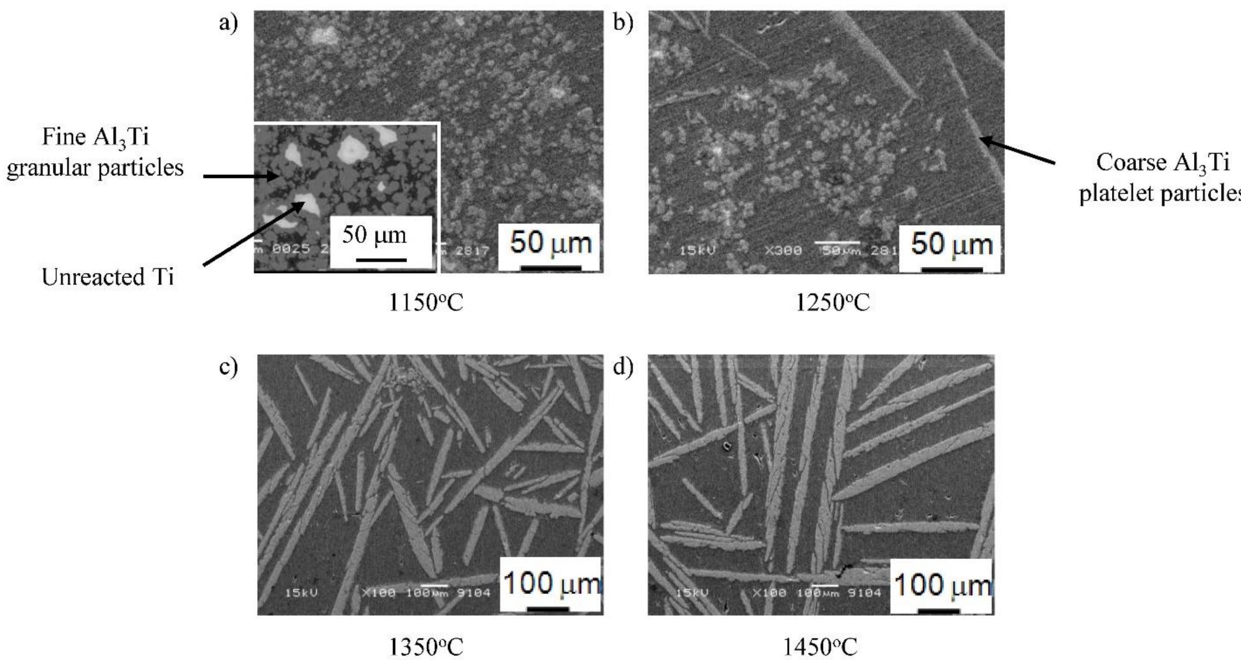

Figure 1.7. Scanning Electron Microcopy (SEM) micrographs of RCMPM-FGMs processed at different temperatures [10].

The porosity, pore size, distribution, and density can be determined through Digital Image Analysis of images extracted from SEM and FESEM and converted to a binary system (Binarization), thereby eliminating false or distorted pores and retaining only the actual pores. This process is performed using specialized software such as Image J or the Image Processing Package (IPP). Subsequently, the number of pores is calculated and their dimensions determined individually, and the surface porosity is derived by dividing the total pore area by the total area of the processed image [10, 16].

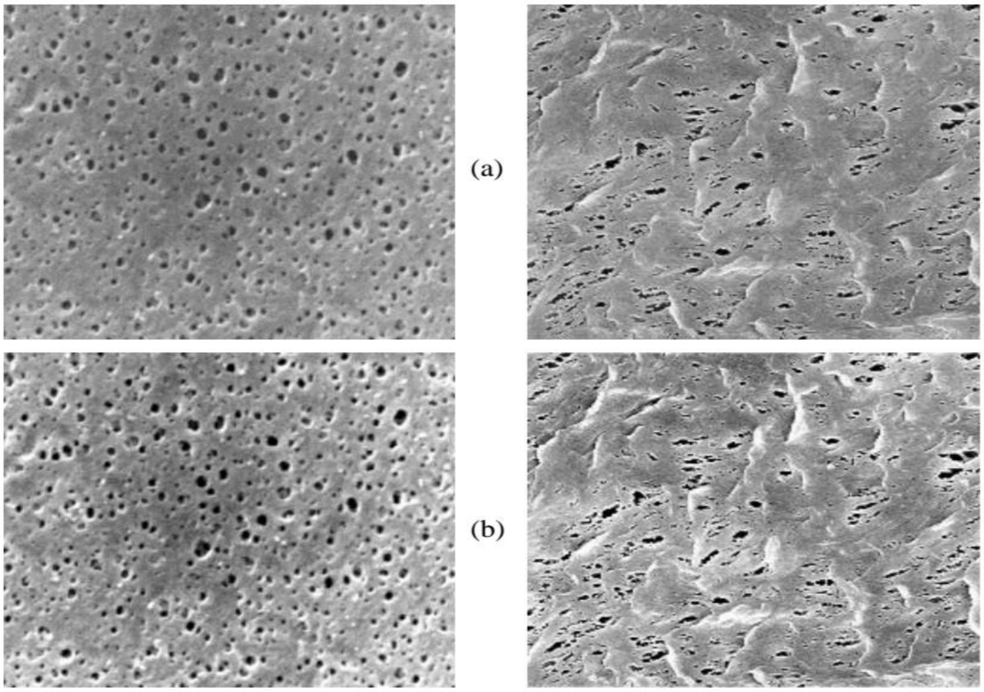

Figure 1.8. FESEM outer images (a) original image; (b) adjusted image[16]

There are also non-destructive techniques such as X-rays or CT scans that detect pores within materials without damaging the sample. A key feature of these techniques is that they can assess the distribution of porosity and estimate its size and shape through three-dimensional analysis using specialized image analysis software such as VG StudioMax [17].

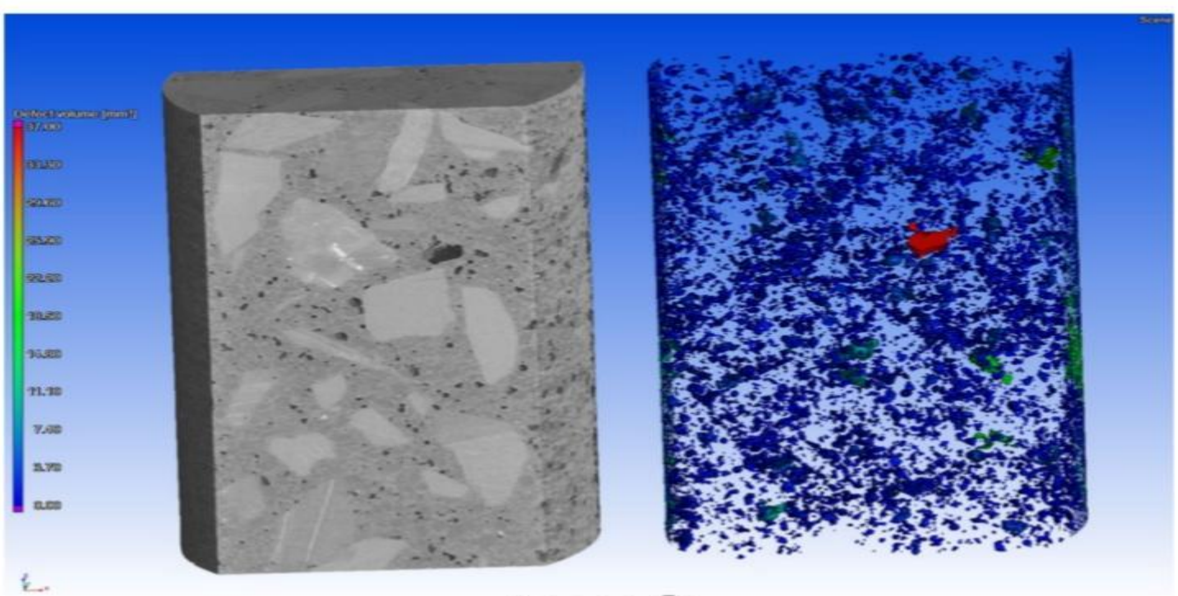

Figure 1.9. 3D view of cylindrical sample cut open virtually with colour-coded voids according to size from the 3D analysis [17].

1.8 Vibration Control

Because vibration control is critical for FGM plate applications, especially those subjected to dynamic loads, active vibration control techniques (Active Vibration Control) that rely on a feedback control system to utilize smart materials, such as piezoelectric materials, as sensors and actuators, either through full or partial (patch) coverage, in order to dampen vibrations and improve dynamic stability[12].

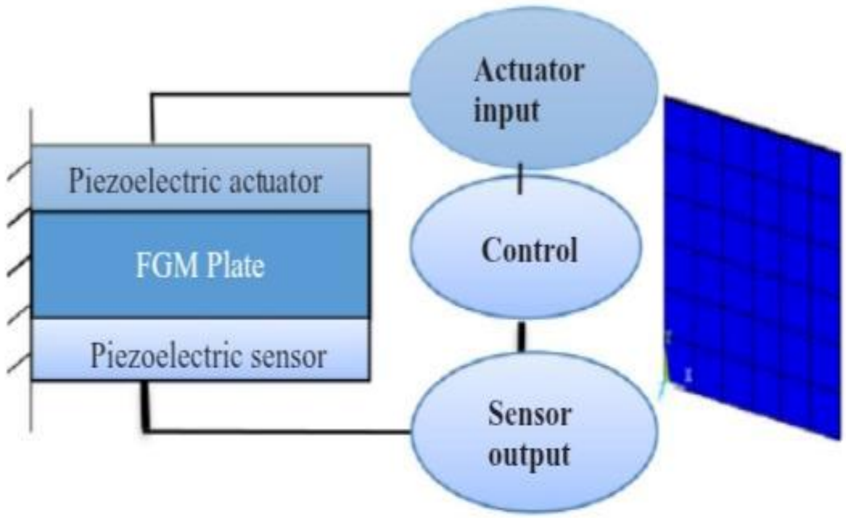

Figure 1.10. Schematic diagram of the active vibration control system utilizing piezoelectric layers [12].

1.9 Application Domains of FGMs

The unique characteristics of functionally graded (FG) materials have attracted significant attention from researchers over the past few decades, fostering their widespread adoption across most engineering fields. Although initially developed for aerospace and aeronautical applications, these advanced materials have successfully expanded into the automotive, biomedical, defense, electrical/electronic, and thermos-electronic industries.

Figure 1.11. The main areas of application of FGM.

1.10 Governing Laws for Material Property Variations in FGM Plates

Functionally Graded Materials (FGMs) are engineered by combining two distinct materials characterized by differing structural and functional properties. Ideally, the transition between these constituents must be continuous—encompassing composition, microstructure, and porosity distribution—to optimize the overall performance of the structure.

FGMs are distinguished by their heterogeneous microstructures, which induce a progressive variation in macroscopic properties throughout the material bulk. This spatial variation is commonly expressed in terms of constituent volume fractions, representing the relative proportion of each phase at any given coordinate. To model these gradients, researchers frequently employ mathematical functions such as the power law, exponential function, or sigmoid function, which enable the representation of a continuous and controlled transition between the constituent phases.

Furthermore, interparticle bonding plays a fundamental role; it must provide sufficient internal structural cohesion to resist fracture while ensuring adequate surface resistance to minimize wear and guarantee long-term material durability (Figure 12).

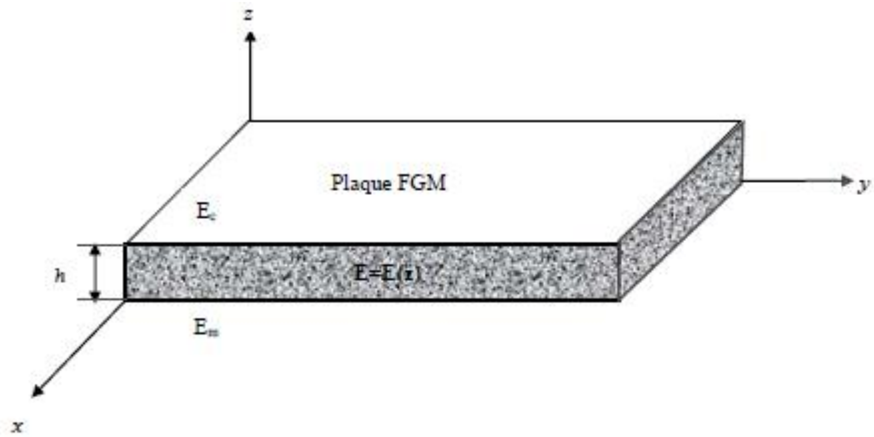

Figure 1.12. Geometric configuration of an FGM plate.

1.11 Material Properties of the P-FGM Plate

The volume fraction of the P-FGM class follows a variation law governed by a power-law function. v(z)= ((z+h/2)/h)^k (1.1)

Where k is a material index (or power-law exponent) and h denotes the plate thickness. Once the local volume fraction v(z)is defined, the effective material properties of the P-FGM plate can be determined via the rule of mixtures.

E(z)= E_m+(E_c+E_m)v(z) (1.2)

E1 and E2 represent the Young's moduli of the bottom (z = -h/2) and top (z = h/2) surfaces of the FGM plate, respectively. The variation of the Young's modulus through the thickness direction of the P-FGM plate is depicted in Figure 1.13. It is clearly observed that the volume fraction changes rapidly near the bottom surface for power-law exponent values of k > 1.

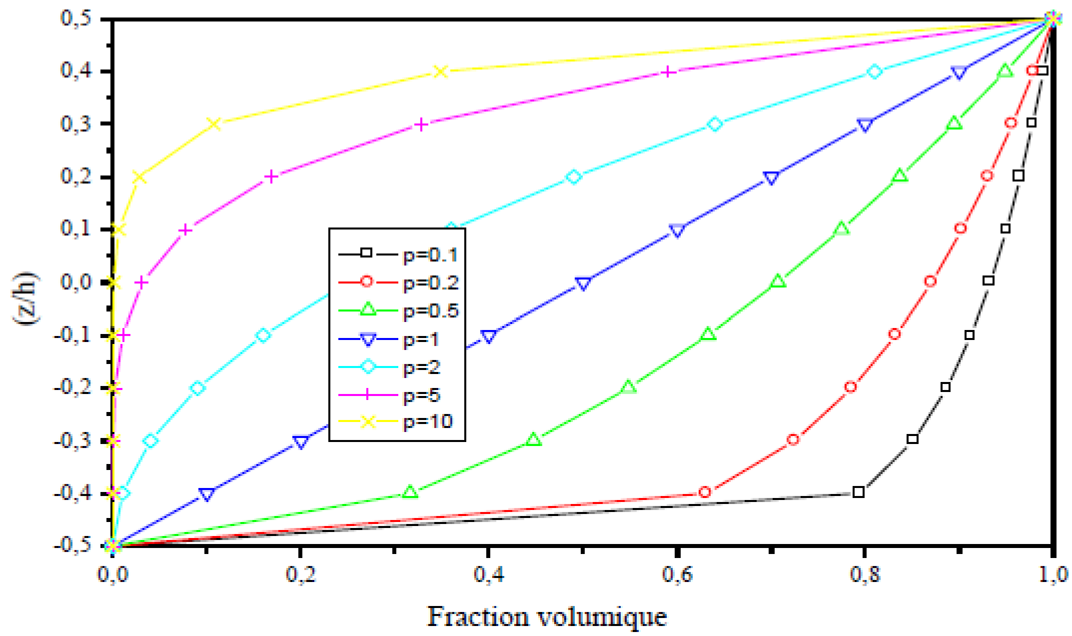

Figure 1.13. Evolution of the volume fraction through the thickness of a P-FGM plate.

1.12 Material Properties of the S-FGM Plate

In the case of adding a P-FGM plate with a single power-law function to a multi-layered composite plate, stress concentrations arise at the interfaces where the material is continuous but changes rapidly. Consequently, Chung and Chi defined the volume fraction of the FGM plate using two power-law functions to ensure a smooth stress distribution across all interfaces.

$$V_1(z) = \frac{1}{2}\left(\frac{\frac{h}{2}+z}{\frac{h}{2}}\right)^k \qquad for -\frac{h}{2} \leq z \leq 0 \qquad (1.3a)$$

$$V_2(z) = 1 - \frac{1}{2}\left(\frac{\frac{h}{2}-z}{\frac{h}{2}}\right)^k \qquad for\ 0 \leq z \leq \frac{h}{2} \qquad (1.3b)$$

Using the rule of mixtures, the Young's modulus of the S-FGM plate can be calculated using the following relations:

$$E(z) = V_1(z)E_1 + [1 - V_1(z)]E_2 \quad for\ -\frac{h}{2} \leq z \leq 0 \ (1.4a)$$

$$E(z) = V_2(z)E_1 + [1 - V_2(z)]\,E_2 \quad for\ \ 0 \leq z \leq \frac{h}{2} \quad (1.4b)$$

Figure 1.14 shows that the volume fraction variation in equations (I.4.a) and (I.4.b) represents sigmoid distributions; in this case, this FGM plate is referred to as an "S-FGM plate.

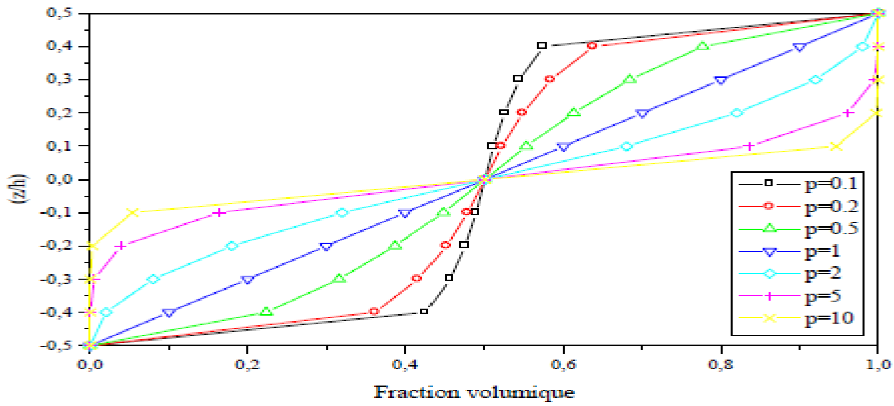

Figure 1.14. Variation of the volume fraction in an "S-FGM" plate.

1.13 Material Properties of the E-FGM Beam

To describe the material properties of FGMs, most researchers employ the exponential function (E-FGM). This exponential distribution of material properties is generally expressed in the form established by Delale and Erdogan (1983).

$$E(z) = E_2 e^{B\left(z+\frac{h}{2}\right)} \qquad (1.5a)$$

With $$B = \frac{1}{2}\ln\left(\frac{E_1}{E_2}\right) \qquad (1.5b)$$

The variation of Young's modulus through the thickness of the E-FGM plate is illustrated in Figure 1.15.

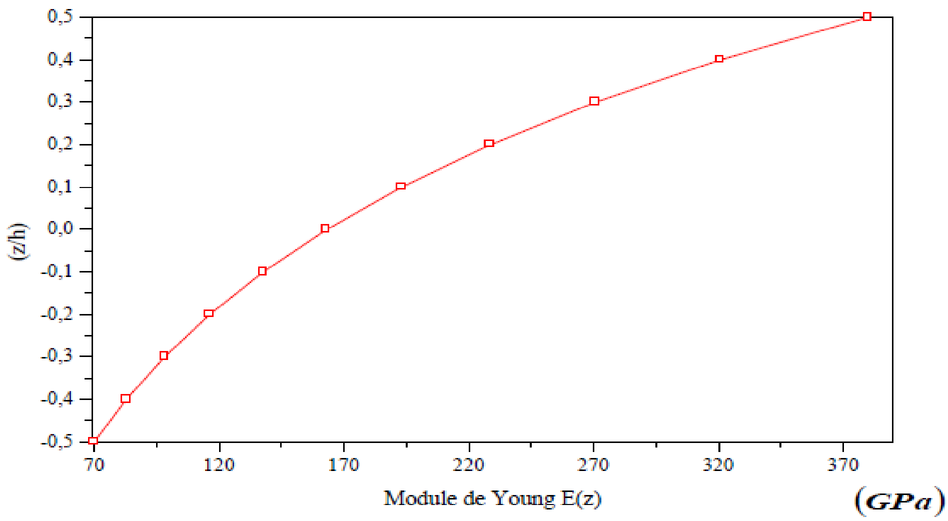

Figure 1.15. Evolution of the Young's modulus in an E-FGM plate.

1.14 Conclusion

In this chapter, we have presented functional gradient materials (FGMs), their characteristics and their fields of application. The different laws governing the variation of their properties are also presented.

Chapitre II :

Introduction to Plate Theories

2.1 Introduction

Modeling the behavior of Functionally Graded Materials (FGMs) is essential to understanding their response under various loading conditions, which requires the use of theories capable of accurately describing their deformation. These theories are primarily classified based on assumptions regarding the distribution of transverse shear stresses through the thickness [3,4].

The Classical Plate Theory (CPT), based on Kirchhoff's hypotheses, is the simplest approach [3,4]. The First-order Shear Deformation Theory (FSDT), associated with Mindlin's work, represented a significant advancement, making it suitable for moderately thick plates, though it requires shear correction factors [3,4]. On the other hand, Higher-order Shear Deformation Theories (HSDTs) eliminate the need for correction factors, thereby achieving the highest levels of accuracy, particularly for thick plates [3,4][20].

This chapter presents the theoretical foundations and accuracy limitations of each theory, supported by a comparative table, and concludes with an examination of the most significant practical applications that demonstrate the concrete value of these materials in engineering [1].

2.2 Theories of FGM Plate Analysis

2.2.1 Classical Love–Kirchhoff Models (Classical Laminated Plate Theory - CLPT)

We begin with the simplest and most general model, known as the Love–Kirchhoff model. This model is based on a linear displacement distribution through the thickness, as described by Reissner (1961). The underlying Love–Kirchhoff hypothesis (1850) assumes a state of plane stress, where transverse shear deformations are neglected. Consequently, a straight line originally normal to the plate's mid-plane remains straight and perpendicular to it after deformation (Figure 2.1).

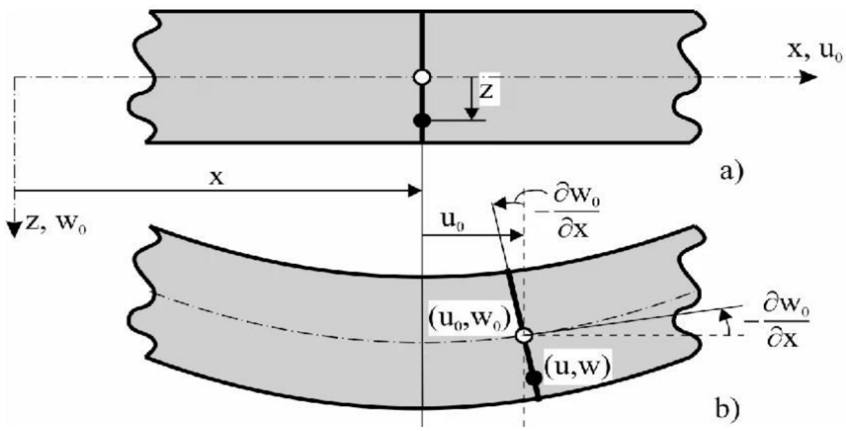

Figure 2.1. An illustration of the CPT theorem [19].

The Love-Kirchhoff displacement field can then be written,

$$\begin{aligned} U_\alpha(x_1,x_2,x_3) &= u_\alpha^0(x_1,x_1) - x_3 \cdot w_{,\alpha}(x_1,x_2); \alpha = 1,2 \\ U_3(x_1,x_2,x_3) &= w(x_1,x_2) \end{aligned} \tag{2.1}$$

with,

u_α^0 : the membrane displacement in the direction α

w : Deflection

$w_{,\alpha}$: The bending rotation (neglecting shear)

A plate is considered thin when the deflection induced by shear deformations remains negligible compared to the deflection generated by the plate's curvature. In the case of a homogeneous isotropic plate, the shear contribution to the total deflection is directly related to the slenderness ratio (L/h). The Classical Plate Theory (CPT) for thin plates is based on the Love–Kirchhoff hypotheses, which state that a straight line normal to the plate's mid-plane remains perpendicular to it after deformation (Figure 2.2). This is equivalent to neglecting the effects of transverse shear deformation.

The displacement field is given by:

$$U(x,y,z) = U_0(x,y) - z\frac{\delta w_0}{\delta x}$$

$$V(x,y,z) = V_0(x,y) - z\frac{\delta w_0}{\delta x}$$

$$W(x,y,z) = W_0(x,y)$$

With (U_0 , V_0 , W_0) are the displacement field components on the mid-plane of the plate. ($z = 0$)

2.2.2 Reissner-Mindlin models (First-order Shear Deformation Theory - FSDT):

Transverse shear cannot be neglected; its consideration is adopted by Mindlin, whose kinematic assumption is as follows: The normal remains straight but not perpendicular to the mid-surface (due to the transverse shear effect) in the deformed configuration (Figure 2.2). The Reissner-Mindlin displacement field is written as:

$$\begin{cases} u_\alpha(x_1, x_2, x_3 = z) = u_\alpha^0(x_1, x_2) - z\phi_{,\alpha}(x_1, x_2) \\ u_3(x_1, x_2, x_3 = z) = w(x_1, x_2) \end{cases} \tag{2.2}$$

with,

ϕ_α *the rotation of the normal to the mid-plane around the axes.* x_α *,*

$\gamma_\alpha^0 = (w_{,\alpha} + \phi_\alpha)$*: The transverse shear strain measured on the mid-plane*

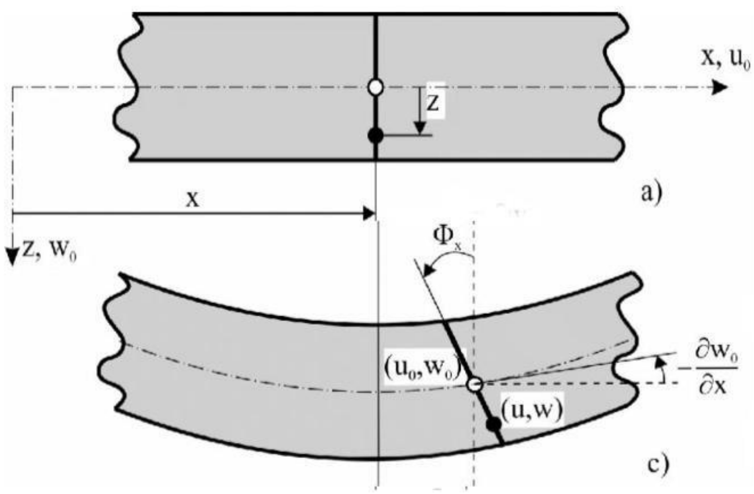

Figure 2.2. An illustration of the FSDT theorem [19].

The FSDT describes the plate kinematics by introducing rotations that are independent of the mid-surface slope and by allowing non-zero transverse shear strains, unlike the classical shear-free theory. These assumptions lead to a displacement field that is linear through the thickness for the in-plane components, and to transverse shear forces integrated into the two-dimensional plate equations. The first-order theory is based on the following displacement field:

$$Uy(x, y, z) = U_0(x, y) - z\emptyset_x(x, y)$$

$$V(x, y, z) = V_0(x, y) - z\emptyset_y(x, y)$$

$$W(x, y, z) = W_0(x, y)$$

With: (U_0, V_0) and ($\emptyset_x$ et $\emptyset_y$) are the membrane displacements, is the transverse displacement, and are the rotations about the y and x axes, respectively.

2.2.2 Higher-Order Shear Deformation Theory (HSDT)

The High-Order Shear Deformation Theory (HSDT) extends the First-Order Shear Deformation Theory (FSDT) to capture the transverse shear stress profile across the plate thickness with high fidelity, especially in thick plate regimes. HSDT relaxes the classical Kirchhoff-Love and Reissner-Mindlin constraints by assuming that lines originally normal to the undeformed mid-surface exhibit non-linear warping post-deformation, thus inducing a non-uniform shear stress state [3]. A major advantage of this higher-order kinematic model is the natural elimination of shear correction factors. Notably, Reddy's third-order framework ensures a quadratic variation of shear stresses through the thickness, while naturally fulfilling the traction-free boundary conditions at the top and bottom faces [3].

Depending on the choice of the kinematic shape function, alternative HSDT variants have been developed, including the Reddy, Touratier, and Karama models [20]. Among equivalent single-layer theories, HSDT demonstrates unparalleled accuracy for thick structures, yielding significantly improved predictions for the structural response of functionally graded material (FGM) plates [3,4].

The displacement field is given as follows:

With: (U0, V0, W0) and (ϕx, ϕy) are the membrane displacements and the rotations about the x and y axes, respectively.

A transverse shear function characterizing the corresponding theories. Indeed, the displacements of the classical plate theory (CPT) are obtained by setting $\Psi(z) = 0$, whereas the first-order shear deformation theory (FSDT) can be obtained by setting $\Psi (z) = z$.

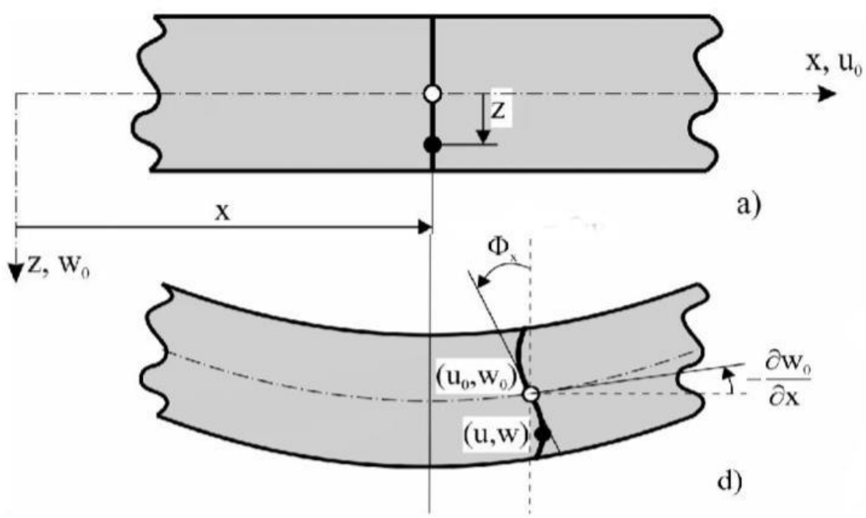

Figure 2.3. An illustration of the HSDT theorem [19].

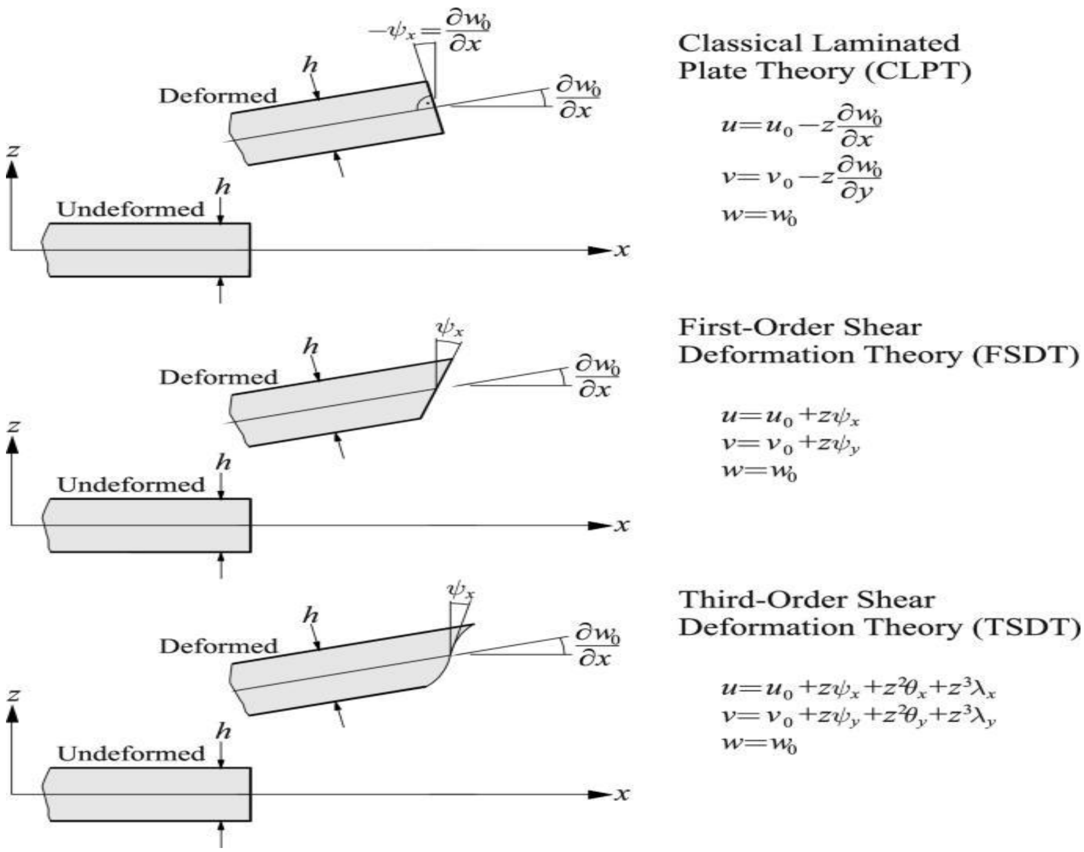

Figure 2.4. The differences between theories in terms of hypotheses and equations [9]

2.3 Conclusion

This chapter presents an overview of the different theoretical plate models, notably the classical Love-Kirchhoff theory (CPT) for the study of thin plates, and the first-order shear deformation theory (FSDT) which accounts for transverse shear effects. In order to obtain accurate results with these theories, shear correction factors are generally introduced. The higher-order shear deformation theory (HSDT) does not require a correction factor and ensures a non-linear distribution through the thickness.

Chapitre III :

Theoretical Formulation

3.1 Introduction

In the present work, analyzing the vibratory behavior of functionally graded material (FGM) plates is of paramount importance for their structural application in severe dynamic environments. This chapter focuses on the free vibration analysis of FGM plates simply supported on all four sides, by combining a five-variable higher-order shear deformation theory (HSDT) with the Navier analytical solution. The developed model is based on a sinusoidal shape function and accounts for the effects of rotary inertia and shear deformations. The governing equations are derived by applying Hamilton's principle, and then expanded into double Fourier series to accurately satisfy the simply supported boundary conditions. The validity of the dimensionless frequencies obtained by the present theory is verified against those from two other theories in the literature, namely FSDT and HSDT, for different values of the side-to-thickness ratio (a/h) and the volume fraction index (p). The effect of porosity distribution is also examined by comparing different pore distribution profiles through the thickness.

3.2 Theoretical Formulation

3.2.1. Material Model

In the present work, we consider a thick rectangular plate of length a, width b, and thickness h, as illustrated in Figure 3.1, along with a Cartesian coordinate system (x, y, z) centered at the mid-plane (z = 0). The plate is made of a functionally graded material (FGM) whose mechanical properties (Young's modulus''E''and density''ρ'') vary continuously through the thickness according to a power-law distribution. For a perfect plate without porosity, effective property P is expressed as:

$$P(z) = P_m + (P_c - P_m)\left(\frac{1}{2} + \frac{z}{h}\right)^p \qquad (3.1)$$

Where the subscripts c and m refer to the ceramic and metal constituents, respectively, and p is the volume fraction index that governs the material variation across the thickness.

To account for the effect of porosities, a porosity volume fraction ε (0≤ε≤ 1) is introduced. In agreement with experimental findings, the porosities tend to concentrate within the mid-plane region of the plate, resulting in a non-uniform distribution. Consequently, the modified material properties are expressed in the following general form:

$$P = P_m + (P_c - P_m)\left(\frac{1}{2}+\frac{z}{h}\right)^P - \frac{\varepsilon}{2}(P_c + P_m)V_j \qquad (3.2)\ )$$

where V(z) signifies the thickness-wise porosity distribution profile. Here, four alternative porosity patterns are investigated:

· Pattern A (uniform distribution): VA=1

· Pattern B (mid-zone localized porosity): VB= 1 -2|z|/h

· Pattern C (top/bottom localized porosity): VC=2|z|/h

· Pattern D (linear asymmetric distribution): VD=1/2-z/h

Setting ε=0 recovers the ideal perfect material distribution given by Eq. (3.1).

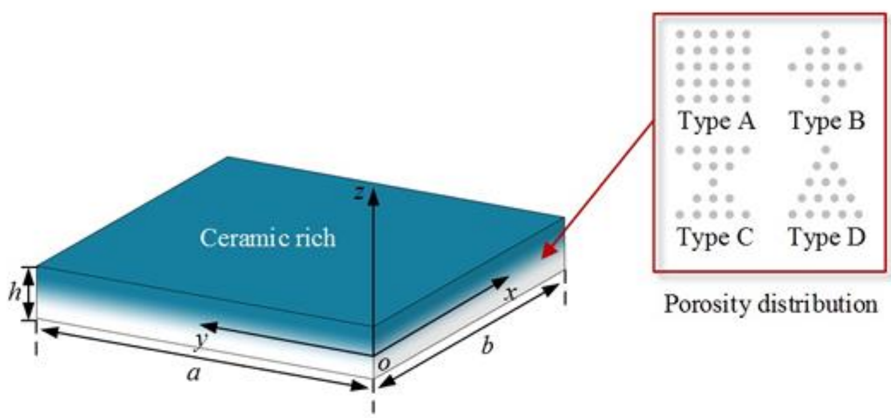

Figure 3.1. Geometric models of porous FGM plats with different structures.

3.2.2. Kinematic Displacement Field

To properly capture the transverse shear deformation and rotational inertia effects, a five-variable high-order shear deformation theory (HSDT) is employed. The displacement field at an arbitrary point (x, y, z) and time t is defined as:

$$u(x,y,z,t) = u_0(x,y,t) - z\frac{\partial w_0}{\partial x} - f(z)\frac{\partial \theta}{\partial x}$$

$$v(x,y,z,t) = v_0(x,y,t) - z\frac{\partial w_0}{\partial y} - f(z)\frac{\partial \theta}{\partial y} \qquad (3.3)$$

$$w(x,y,z,t) \ = \ w_0(x,y,t)$$

Here u_0 and v_0 are the in-plane displacement components of the mid-plane, w_0 denotes the total transverse displacement, and θ represents an additional rotation variable associated with transverse shear deformations. The shape function $f(z)$ is chosen as a sinusoidal function, defined by:

$$f(\mathrm{z}) = \frac{h}{\pi} sin\frac{\pi z}{h} \tag{3.4}$$

major advantage of this choice is that it inherently satisfies the condition $f'\left(\pm\frac{h}{2}\right) = \ 0$, which guarantees zero transverse shear stresses on the top and bottom surfaces of the plate without the need for any shear correction factor.

3.2.3. Strain–Displacement Relations

Under the assumption of small strains, the strain components associated with the displacement field (3.3) are derived as:

$$\varepsilon_x = \frac{\partial u}{\partial x} = \frac{\partial u_0}{\partial x} - z\frac{\partial^2 w_0}{\partial x^2} - f(z)\frac{\partial^2 \theta}{\partial x^2}$$

$$\varepsilon_y = \frac{\partial v}{\partial y} = \frac{\partial v_0}{\partial y} - z\frac{\partial^2 w_0}{\partial y^2} - f(z)\frac{\partial^2 \theta}{\partial y^2}$$

$$\varepsilon_z = \frac{\partial w}{\partial z} = 0 \tag{3.5}$$

$$\gamma_{xy} = \frac{\partial v}{\partial x} + \frac{\partial u}{\partial y}$$

$$\gamma_{xz} = \frac{\partial w}{\partial x} + \frac{\partial u}{\partial z}$$

$$\gamma_{yz} = \frac{\partial w}{\partial y} + \frac{\partial v}{\partial z}$$

3.2.4. Constitutive Equations

Assuming a linear elastic and isotropic behavior at every local point, the stress–strain relationship is written in the following matrix form:

$$\begin{Bmatrix} \sigma x \\ \sigma y \\ \tau xy \\ \tau xz \\ \tau yz \end{Bmatrix} = \begin{bmatrix} Q_{11} & Q_{12} & 0 & 0 & 0 \\ Q_{21} & Q_{22} & 0 & 0 & 0 \\ 0 & 0 & Q_{44} & 0 & 0 \\ 0 & 0 & 0 & Q_{55} & 0 \\ 0 & 0 & 0 & 0 & Q_{66} \end{bmatrix} \begin{Bmatrix} \varepsilon_x \\ \varepsilon_y \\ \gamma_{xy} \\ \gamma_{xz} \\ \gamma_{yz} \end{Bmatrix} \tag{3.6}$$

This relates the stress components $(\sigma_x, \sigma_y, \tau_{xy}, \tau_{yz}, \tau_{xz})$ to the strain components $(\varepsilon_x, \varepsilon_y, \gamma_{xy}, \gamma_{yz}, \gamma_{xz})$ by means of the elastic coefficients $Q_{ij}(z)$, defined as:

$$Q_{11}(z) = Q_{22}(z) = \frac{E(z)}{1-\nu^2} \quad ; Q_{12}(z) = Q_{21}(z) = \frac{\nu E(z)}{1-\nu^2}$$

$$Q_{44}(z) = Q_{55}(z) = Q_{66}(z) = G(z) = \frac{E(z)}{2(1+\nu)} \tag{3.7}$$

where $E(z)$ is the Young's modulus varying across the thickness, and ν is Poisson's ratio, assumed to be constant due to the close values of the ceramic and metal constituents.

3.2.5. Stress Resultants

The stress resultants are obtained by integrating the stresses through the thickness, weighted appropriately. For the in-plane stresses we define:

Where: $z_{max} = +\frac{h}{2} \quad ; z_{min} = -\frac{h}{2}$

And for : $i = (x, y, xy)$

$$N_i = \int_{zmin}^{zmax} \sigma_i dz$$

$$M_i = \int_{zmin}^{zmax} \sigma_i z dz \tag{3.8}$$

$$S_i = \int_{zmin}^{zmax} \sigma_i f(z) dz$$

The generalized transverse shear forces are defined using the derivative of the shape function:

$$N_{xz} = \int_{zmin}^{zmax} \tau_{xz} f'(z) dz \qquad N_{yz} = \int_{zmin}^{zmax} \tau_{yz} f'(z) dz \tag{3.9}$$

By substituting the strain–displacement relations (3.5) into the constitutive equations (3.6) _ (3.7), and then into the definitions of the stress resultants (3.8) and (3.9), and performing the integration over the thickness, the constitutive equations of the plate are expressed in terms of the generalized strains and curvatures of the mid-plane. The following stiffness constants naturally appear:

$$\{A_{ij}, B_{ij}, D_{ij}\} = \int_{zmin}^{\text{zmax}} Q_{ij}(1, z, z^2)dz \quad ; (i,j = 1,2,6)$$

$$\{B_{ij}^s, D_{ij}^s, H_{ij}^s\} = \int_{zmin}^{zmax} Qij\big(f(z), zf(z), f^2(z)\big)dz \quad ; (i,j = 1,2,6) \tag{3.10}$$

$$\{A_{ij}^s\} = \int_{zmin}^{zmax} Q_{ij}(f'(z))^2 dz \quad ; \quad (i.j = 4,5)$$

These stiffness constants will be used later to construct the stiffness matrix of the system.

3.2.6. Analytical Navier Solution

For a plate that is simply supported on all four edges (SSSS), the boundary conditions allow an exact solution to be obtained using the Navier method. Accordingly, the displacement unknowns are expanded in double Navier series that satisfy the boundary conditions identically:

$$U_0 = \sum_{m=1}^{\infty}\sum_{n=1}^{\infty} U_{mn} cos\alpha x \; sin\beta y \; e^{i\omega t}$$

$$V_0 = \sum_{m=1}^{\infty}\sum_{n=1}^{\infty} V_{mn} sin\alpha x \; cos\beta y \; e^{i\omega t} \tag{3.11}$$

$$W_0 = \sum_{m=1}^{\infty}\sum_{n=1}^{\infty} W_{mn} sin\alpha x \; sin\beta y \; e^{i\omega t}$$

$$\Theta = \sum_{m=1}^{\infty}\sum_{n=1}^{\infty} \Theta_{mn} sin\alpha x \; sin\beta y \; e^{i\omega t}$$

Where:$\alpha = \frac{m\pi}{a}$ $\quad ; \beta = \frac{n\pi}{b}$

Here m and n denote the mode numbers, $U_{mn}, V_{mn}, W_{mn}, \Theta_{mn}$ are the unknown amplitudes, ω is the natural frequency, and $i = \sqrt{-1}$ is the imaginary unit.

Substituting the series expansions (3.11) into the equations of motion (3.10), and making use of the constitutive relations that connect the stress resultants to the generalized strains and curvatures through the stiffness constants (3.10), yields, after differentiation and term grouping, a homogeneous algebraic system for each pair (m, n). The system can be cast in the following compact matrix form:

$$([\boldsymbol{K}] - \omega^2 [\boldsymbol{M}])\Delta = 0 \tag{3.12}$$

Where $\Delta = \{U_{mn}\ V_{mn}\ W_{mn}\ \theta_{mn}\}^T$ is the vector of unknown amplitudes, and [**K**] and [**M**] are the symmetric stiffness and mass matrices, respectively ($\boldsymbol{k}_{ij} = \boldsymbol{k}_{ji}$; $\boldsymbol{M}_{ij} = \boldsymbol{M}_{ji}$).

The explicit elements of the stiffness matrix [**K**] are:

$$K_{11} = -A_{11}\,\alpha^2 - A_{66}\,\beta^2$$

$$K_{12} = -\alpha\,\beta\,(A_{12} + A_{66})$$

$$K_{13} = \alpha\,[B_{11}\,\alpha^2 + (B_{12} + 2B_{66})\,\beta^2]$$

$$K_{14} = \alpha\,[B^s{}_{11}\,\alpha^2 + (B^s{}_{12} + 2B^s{}_{66})\,\beta^2]$$

$$K_{22} = -A_{66}\,\alpha^2 - A_{22}\,\beta^2$$

$$K_{23} = \beta\,[(B_{12} + 2B_{66})\,\alpha^2 + B_{22}\,\beta^2]$$

$$K_{24} = \beta\,[(B^s{}_{12} + 2B^s{}_{66})\,\alpha^2 + B^s{}_{22}\,\beta^2]$$

$$K_{33} = -D_{11}\,\alpha^4 - 2(D_{12} + 2D_{66})\,\alpha^2\,\beta^2 - D_{22}\,\beta^4$$

$$K_{34} = -D^s{}_{11}\,\alpha^4 - 2(D^s{}_{12} + 2D^s{}_{66})\,\alpha^2\,\beta^2 - D^s{}_{22}\,\beta^4$$

$$K_{44} = -H^s{}_{11}\,\alpha^4 - 2(H^s{}_{12} + 2H^s{}_{66})\,\alpha^2\,\beta^2 - H^s{}_{22}\,\beta^4 - A^s{}_{55}\,\alpha^2 - A^s{}_{44}\,\beta^2$$

The elements of the mass matrix [M] read:

$$M_{11} = I_1$$

$$M_{12} = 0$$

$$M_{13} = -I_2\,\alpha$$

$$M_{14} = -I_4\,\alpha$$

$$M_{22} = I_1$$

$$M_{23} = -I_2\,\beta$$

$$M_{24} = -I_4\,\beta$$

$$M_{33} = I_1 + I_3\,(\alpha^2 + \beta^2)$$

$$M_{34} = I_1 + I_5\,(\alpha^2 + \beta^2)$$

$$M_{44} = I_1 + I_6(\alpha^2 + \beta^2)$$

Equation (3.12) constitutes a standard eigenvalue problem. For a non-trivial solution to exist, the determinant of the coefficient matrix must vanish:

$$det(\,[K] - \omega^2\,[M]) = 0 \tag{3.13}$$

olving this equation yields the natural frequencies ω_{mn} of the plate for each vibration mode (m, n). For presentation and comparison purposes, these frequencies will later be expressed in appropriate dimensionless forms, as shown in the subsequent numerical examples.

3.2.7. Energy Formulation and Equations of Motion

The equations of motion are derived using Hamilton's principle, which states that the time integral of the variation of the difference between kinetic and strain energies vanishes for the true motion:

$$\int_0^t (\delta U - \delta K)dt = 0 \tag{3.14}$$

Where δU and δK denote the variations of the strain energy and the kinetic energy, respectively.

Strain energy variation. The variation of the strain energy for the plate is written as a volume integral of the inner product of stresses and virtual strains:

$$\delta U = \int_V (\,\sigma_x \delta\varepsilon_x + \sigma_y \delta\varepsilon_y + \sigma_z \delta\varepsilon_z + \tau_{xy}\delta\gamma_{xy} + \tau_{xz}\delta\gamma_{xz} + \tau_{yz}\delta\gamma_{yz})dV \tag{3.15}$$

By substituting the strain expressions from (3.5), integrating through the thickness using the stress resultants (3.8)–(3.9), and integrating by parts over the plate area, the variation of the strain energy can be cast into the following compact form:

$$\delta U = \int_V (U_u\,\delta u + U_v\delta v + U_w\delta w + U_\theta\delta\theta) \tag{3.16}$$

Where:

$$U_u = \frac{\partial N_x}{\partial x} + \frac{\partial N_{xy}}{\partial y}$$

$$U_v = \frac{\partial N_{xy}}{\partial y} + \frac{\partial N_y}{\partial y}$$

$$U_w = \frac{\partial^2 M_x}{\partial x^2} + 2\frac{\partial^2 M_{xy}}{\partial xy} + \frac{\partial^2 M_y}{\partial y^2}$$

$$U_\theta = \frac{\partial^2 S_x}{\partial x^2} + 2\frac{\partial S_{xy}}{\partial_{xy}} + \frac{\partial S_y}{\partial y^2} + \frac{\partial N_{xz}}{\partial x} + \frac{\partial N_{yz}}{\partial y}$$

Kinetic energy variation. The variation of the kinetic energy is given by:

$$\delta K = \int_A \int_{zmin}^{zmax} (\dot{u}\delta\dot{u} + \dot{v}\delta\dot{v} + \dot{w}\delta\dot{w})dAdzd \tag{3.17}$$

Substituting the displacement field (3.3) into (3.15), integrating over the thickness, and introducing the mass inertias:

$$(I_1, I_2, I_3, I_4, I_5, I_6) = \int_{zmin}^{zmax} \rho(z)\big(1, z, z^2, f(z), zf(z), f^2(z)\big)dz \tag{3.18}$$

$$\delta K = \int_A (\,K_u\delta u + K_v\delta v + K_w\delta w + K_\theta\delta\theta) \tag{3.19}$$

With:

$$K_u = I_1\ddot{u}_0 - I_2\frac{\partial \ddot{w}_0}{\partial x} - I_4\frac{\partial\ddot{\theta}}{\partial x}$$

$$k_v = I_1 \ddot{v}_0 - I_2 \frac{\partial \ddot{w}_0}{\partial y} - I_4 \frac{\partial \ddot{\theta}}{\partial y}$$

$$K_w = I_1 \ddot{w}_0 - I_2 \left(\frac{\partial \ddot{u}_0}{\partial x} + \frac{\partial \ddot{v}_0}{\partial y}\right) - I_3 \left(\frac{\partial \ddot{w}}{\partial x^2} + \frac{\partial \ddot{w}}{\partial y^2}\right) - I_5 \left(\frac{\partial \ddot{\theta}}{\partial x^2} + \frac{\partial \ddot{\theta}}{\partial y^2}\right)$$

$$K_\theta = I_4 \left(\frac{\partial \ddot{u}_0}{\partial x} + \frac{\partial \ddot{v}_0}{\partial y}\right) - I_5 \left(\frac{\partial \ddot{w}_0}{\partial x^2} + \frac{\partial \ddot{w}_0}{\partial y^2}\right) - I_6 \left(\frac{\partial \theta}{\partial x^2} + \frac{\partial \theta}{\partial y^2}\right)$$

Equations of motion. Applying Hamilton’s principle (3.11), integrating by parts with respect to time, and setting the coefficients of the independent virtual variations δu_0,δv_0,δw_0, and $\delta\theta$ to zero separately, we derive the four differential equations of motion:

$$\begin{aligned} \delta u_0 &: \quad U_u = K_u \\ \delta v_0 &: \quad U_v = K_v \\ \delta w_0 &: \quad U_w = K_w \\ \delta \theta &: \quad U_\theta = K_\theta \end{aligned} \tag{3.19}$$

These equations, together with the definitions of the stress resultants, the stiffness constants (3.10), and the mass inertias (3.16), constitute the governing system for the free vibration analysis of the FG plate.

3.3 Conclusion

This chapter established the complete theoretical formulation for the free vibration analysis of porous FGM plates. A five-variable higher-order kinematic theory, combined with a sinusoidal shape function, was developed to accurately model the warping of cross-sections without requiring a shear correction factor. The equations of motion were derived using Hamilton's principle and then solved analytically via the Navier method for simply supported boundary conditions. The expressions of the stiffness and mass matrices were explicitly formulated as functions of the material properties, porosity gradient, and volume fraction indices. This formulation will serve as a robust foundation for the parametric studies and validations presented in the following chapters.

Chapitre IV:

Results and Discussion

4.1 Introduction

This chapter is dedicated to the presentation, analysis, and discussion of the numerical results derived from the mathematical model developed in the previous chapters. The primary objective is to characterize the vibratory behavior of porous plates by evaluating the influence of various geometric and material parameters on their natural frequencies of vibration. The originality of this study relies on the application of a higher-order trigonometric kinematic theory, which accurately models the warping of cross-sections without resorting to shear correction factors. First, a crucial validation step is carried out to verify the accuracy and reliability of our analytical approach (based on the Navier solution) by comparing our dimensionless frequencies with those from the literature for homogeneous, FGM, and porous plates. Subsequently, a comprehensive parametric study is performed to analyze the combined impact of: The porosity distribution and coefficient through the thickness; The side-to-thickness ratio (slenderness ratio a/h) and the aspect ratio (a/b) of the plate; The volume fraction index (p) of the functionally graded material (FGM).The in-depth physical discussions arising from these results aim to provide useful guidelines for the optimal design of lightweight and porous plate structures subjected to severe dynamic environments.

4.2 Presentation and analysis of results:

In this section, three validity verifications are carried out on the computations of the proposed theory.

La plaque étudiée est une plaque carrée fonctionnellement gradient, simplement appuyée sur les quatre bords (condition SSSS), avec une longueur a, une largeur b telle que a=b, et une épaisseur h. Les propriétés mécaniques évoluent selon une loi de puissance à travers l’épaisseur, reliant les caractéristiques du métal et de la céramique constituante,

The following dimensionless quantities are introduced for the study:

$$\widehat{\omega} = \omega h\sqrt{\frac{\rho_c}{E_c}} \;\; ; \; \overline{\omega} = \omega \frac{a^2}{h}\sqrt{\frac{\rho_c}{E_c}} \qquad (4.1)$$

The modified material properties are expressed in the following general form:

$$P = P_m + (P_c - P_m)\left(\frac{1}{2} + \frac{z}{h}\right)^P - \frac{\varepsilon}{2}(P_c + P_m)V_j$$

To examine the accuracy of the proposed formulation, the fundamental dimensionless To examine the accuracy of the proposed formulation, the fundamental dimensionless frequency $\hat{\omega}$ of a fully simply supported square Al/Al_2O_3 plate is first evaluated for various values of the power-law index p and thickness ratio a/h. The results are compared in Table 4.1 with predictions from the literature based on FSDT and HSDT.

Table 4.1. Comparison of the first four nondimensional frequencies $\omega\hat{}$ of square plate (b=2a):

a/h	Methode	Powr lew index(p)				
		0	0.5	1	4	10
5	FSDT	0.2112	0.1805	0.1631	0.1397	0.1324
	HSDT	0.2113	0.1807	0.1631	0.1378	0.1301
	Present	0.2112	0.1807	0.1631	0.1377	0.1300
10	FSDT	0.0577	0.0490	0.0442	0.0382	0.0366
	HSDT	0.0577	0.0490	0.0442	0.0381	0.00364
	Present	0.0576	0.0441	0.0441	0.0380	0.0363
20	FSDT	0.0148	0.0125	0.0113	0.0098	0.0094
	HSDT	0.0148	0.0125	0.0113	0.0098	0.0094
	Present	0.0147	0.0125	0.0113	0.0098	0.0094

The comparative evaluation is extended to a rectangular plate with b = 2a. Table 4.2 summarizes the first four dimensionless frequencies $\bar{\omega}$ for different vibration modes (m, n), power-law indices p, and thickness ratios a/h, as obtained from the present theory and from reference TSDT and FSDT solutions. This step verifies the validity of the adopted sinusoidal shape function for higher modes and different aspect ratios.

Table 4.2. Comparison of non-dimensional fundamental frequency of square plate (2a=b):

a/h	Mode (m,n)	Method	Power law index(P)						
			0	0.5	1	2	5	8	10
5	1(1,1)	FSDT	3.4409	2.9322	2.6473	2.4017	2.2528	2.1985	2.1677
		TSDT	3.4412	2.9347	2.6475	2.3949	2.2272	2.1697	2.1407
		Present	3.4416	2.9349	2.6477	2.3947	2.2259	2.1688	2.1402
	2(1,2)	FSDT	5.2802	4.5122	4.0773	3.6953	3.4492	3.3587	3.3094
		TSDT	5.2813	4.5180	4.0781	3.6805	3.3938	3.2964	3.2514
		Present	5.2822	4.5186	4.0786	3.6804	3.3913	3.2947	3.2505
	3(1,3)	FSDT	8.0710	6.9231	6.2636	5.6695	5.2579	5.1045	5.0253
		TSDT	8.0749	6.9366	6.2663	5.6390	5.6390	4.9758	4.9055
		Present	8.0771	6.9383	6.2677	5.6390	5.1378	4.9726	4.9043
	4(2,1)	FSDT	9.7416	8.6926	7.8711	7.1189	6.5749	5.9062	5.02518
		TSDT	10.1164	8.7138	7.8762	7.0751	6.4074	6.1846	6.0954
		Present	10.1201	8.7166	7.8787	7.0756	6.4010	6.1805	6.0941
10	1(1,1)	FSDT	3.6518	3.0983	2.7937	2.5386	2.3998	2.3504	2.3197
		TSDT	3.6518	3.0990	2.7937	2.5364	2.3916	2.3411	2.3110
		Present	3.6518	3.0990	2.7937	2.5364	2.3912	2.3407	2.3108
	2(1,2)	FSDT	5.7693	4.8997	4.4192	4.0142	3.7881	3.7072	3.6586
		TSDT	5.7694	4.9014	4.4192	4.0090	3.7682	3.6846	3.6368
		Present	5.7696	4.9016	4.4193	4.0088	3.7672	2.3108	3.6364
	3(1,3)	FSDT	9.1876	7.8145	7.0512	6.4015	6.0247	5.8887	5.6580
		TSDT	9.1880	7.8189	7.0515	6.3886	5.9765	5.8341	5.7575
		Present	9.1886	7.8194	7.0518	6.3884	5.9741	5.8324	5.7566
	4(2,1)	FSDT	11.8310	10.0740	9.0928	8.2515	7.7505	7.5688	7.4639
		TSDT	11.8315	10.0810	9.0933	8.2309	7.6731	7.4813	7.3921
		Present	11.8325	10.0818	9.0940	8.2306	7.6695	7.4786	7.3808
20	1(1,1)	FSDT	3.7123	3.1456	2.8352	2.5777	2.4425	2.3948	2.3642
		TSDT	3.7123	2.8352	2.8352	2.5771	2.4403	2.3923	2.3619
		Present	3.7123	3.1458	2.8352	2.5770	2.4401	2.3921	2.3618
	2(1,2)	FSDT	5.9198	5.0175	4.5228	4.1115	3.8939	3.8170	3.7681
		TSDT	5.9199	5.0180	4.5228	4.1100	3.8884	3.8107	3.7622
		Present	5.9199	5.0179	4.5228	4.1100	3.8880	3.8105	3.7621
	3(1,3)	FSDT	9.5668	8.1121	7.3132	6.6471	6.2903	6.1639	6.0848
		TSDT	9.5669	8.1133	7.3132	6.6433	6.2760	6.1476	6.0690
		Present	9.5670	8.1134	7.3133	6.6432	6.2753	6.1470	6.0687
	4(2,1)	FSDT	12.4560	10.5660	9.5261	8.6572	8.1875	8.0207	7.9166
		TSDT	12.4562	10.5677	9.5261	8.6509	8.1636	7.9934	7.8909
		Present	12.4565	10.5679	9.5263	8.6507	8.1623	7.9924	7.8904

The influence of porosity is now examined. Table 4.3 presents the variation of the dimensionless frequency $\bar{\omega}$ with the porosity volume fraction ε for two different porosity distribution patterns, namely Type A (uniform) and Type B (mid-zone localized). Different values of the power-law index p and two thickness ratios (a/h = 5 and a/h = 10) are considered, in order to highlight the combined effect of porosity level, porosity distribution, and material gradation on the vibration response.

Table 4.3. Comparison of the first four no dimensional frequencies $\hat{\omega}$ of a=b;h=1;

a/h	Prosite	P=0		P=0.5		P=1	
		Type A	Type B	Type A	Type B	Type A	Type B
5	0	5.2822	5.2822	4.5186	4.5186	4.0786	4.0786
	0.2	5.4122	5.4122	4.5101	4.5977	3.8825	4.0995
	0.4	5.6895	5.5617	4.4711	4.6873	3.3987	4.1115
10	0	5.7696	5.7696	4.9016	4.9016	4.4193	4.4193
	0.2	5.9501	5.9334	4.8820	5.0063	4.1875	4.4595
	0.4	6.2146	6.1239	4.8223	5.1277	3.6290	4.4945

4.3 Effect of porosity and gradient index:

This section discusses how various porosity and gradient in dexes affect the non-dimensional frequency of FGM plates, four distribution types (type A, B, C and D), six gradient in dexes (p = 0, 1, 2, 3, 4, 5) and four porosities (λ_0 = 0, 0.1, 0.2, 0.3) are taken into account. Also, fixed aspect ratio a/b = 1, width-to-thickness ratio a/h = η = 5.

The results show that the dimensionless frequency decreases with the increase of the gradient index p and the porosity coefficient λ0. This decrease is due to the reduction in stiffness of the P-FGM plates caused by the increase in the metallic fraction and pores. The VA distribution exhibits the highest sensitivity to porosity, with a significant drop in frequencies. Conversely, the VB and VC distributions offer a more stable behavior and higher frequencies. Thus, the porosity distribution strongly influences the vibrational characteristics of P-FGM plates.

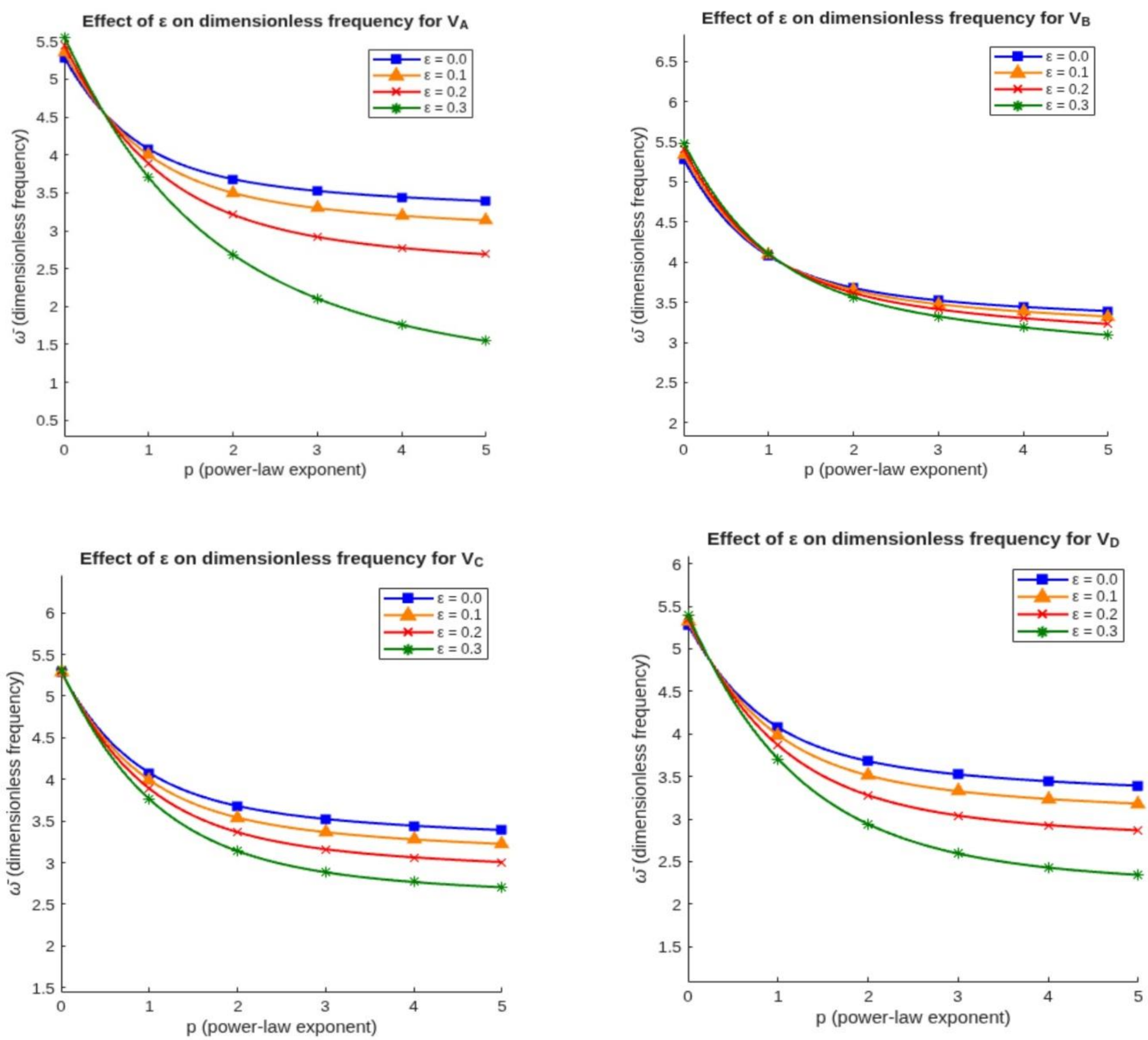

Figure 4.1. Effect of porosity and gradient index on the frequency value of P-FGM plates under type A, B, C, D distribution.

Table 4.4: Properties of Ceramic and Metallic Materials.

Matièr	E	ν	ρ
Al_2O_3	350	0.26	3800
Sic	302	0.17	3100
Si_3N_4	348,45	0.24	2370

The results show that the dimensionless frequency $\hat{\omega}$ gradually decreases with the increase of the gradient index p for all porosity distributions VA, VB, VC, and VD. This decrease reflects the reduction in stiffness of the FGM plates as the metallic fraction becomes more significant. It is also observed that the ceramic material strongly influences the vibrational behavior:
Al_2O_3 reinforced plate's exhibit the highest frequencies, followed by
Sic, while Si_3N_4 yields the lowest values. The VB and VC distributions provide better dynamic stability compared to the VA and VD cases. Thus, the choice of ceramic material and the type of porosity distribution play an essential role in the vibrational performance of P-FGM plates.

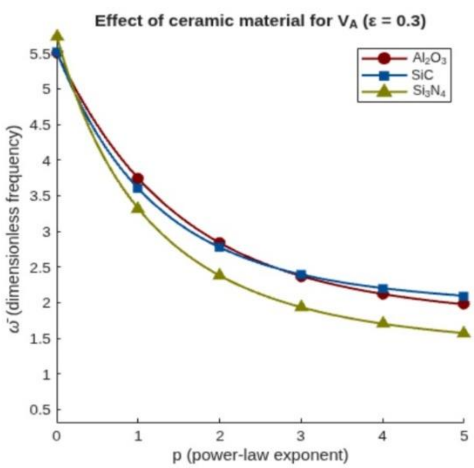

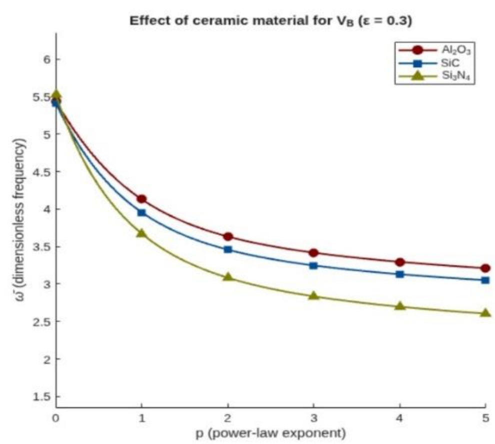

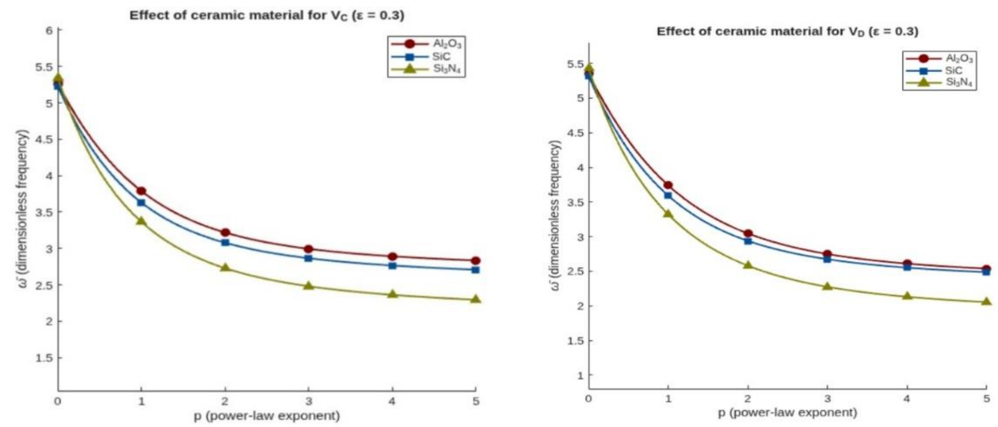

Figure 4.2. Effect of porosity distribution pattern on dimensionless frequency $\bar{\omega}$ for patterns A, B, C, and D (a/h = 5, ε = 0.3)

The results in Figure 4.5 show that the dimensionless frequency $\bar{\omega}$ increases with the increase of the aspect ratio a/h for all porosity distributions VA, VB, VC, and VD. This increase is linked to the enhancement of the bending stiffness of the plates as the thickness becomes relatively smaller. It is also noted that the different porosity distributions influence the vibrational behavior in distinct ways: the VB and VC distributions generally present higher and more stable frequencies, whereas VA and VD show greater sensitivity to porosity effects. For $Al_2\ O_3$, the frequencies remain relatively high due to the significant stiffness of this ceramic material. Thus, the geometric aspect ratio a/h and the type of pore distribution play an essential role in the dynamic response of P-FGM plates.

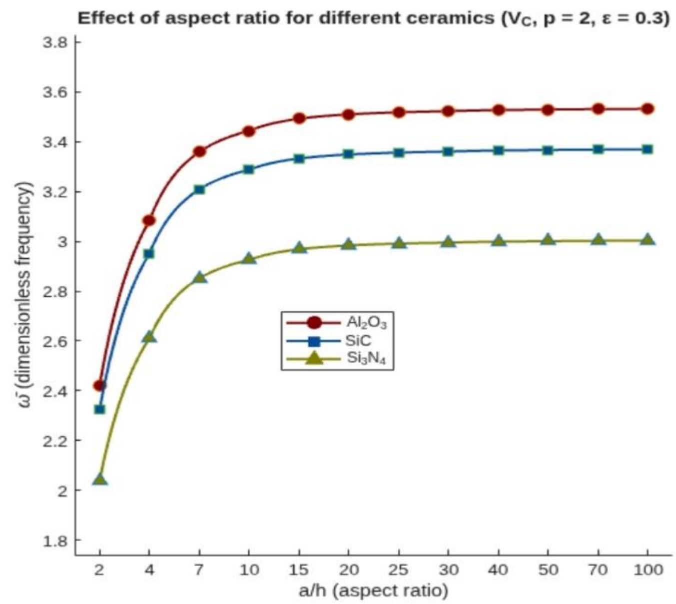

Figure 4.3. Effect of aspect ratio a/h on dimensionless frequency $\bar{\omega}$ for Al_2O_3 (p = 2, ε = 0.3) for porosity distribution patterns A, B, C, and D

For a low aspect ratio (a/h < 2), the dimensionless frequency $\bar{\omega}$ increases with a/h due to the dynamic stiffening effect. Beyond a/h > 2, $\bar{\omega}$ reaches a plateau, indicating that the geometric influence becomes negligible compared to the intrinsic properties of the material. Among the three ceramics, Al_2O_3 systematically exhibits the highest frequencies, followed by SiC and Si_3N_4, due to its more favorable Young's modulus-to-density ratio. At a fixed porosity (ε =0.3), the material hierarchy remains stable regardless of the pore distribution pattern (A, B, C, D).

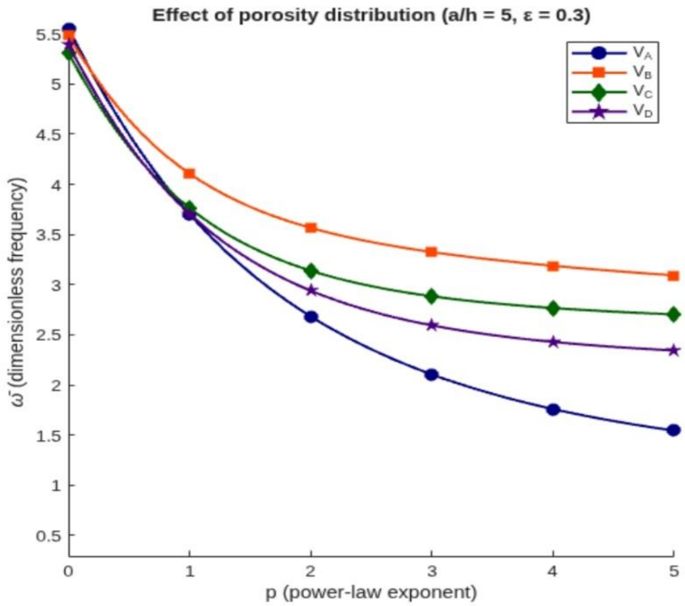

Figure 4.4. Effect of ceramic material on dimensionless frequency $\bar{\omega}$ for porosity distribution patterns A, B, C, and D (ε = 0.3)

For a low aspect ratio (a/h < 2), the dimensionless frequency $\bar{\omega}$ increases rapidly with a/h, reflecting a dynamic stiffening effect. Beyond a/h > 2, $\bar{\omega}$ reaches a plateau, indicating that the geometric influence becomes negligible compared to the intrinsic properties of the materials. Al_2O_3 exhibits the highest frequencies, followed by SiC and then Si_3N_4, due to its more favorable Young's modulus-to-density ratio. Porosity pattern C, at ε = 0.3, allows maximizing the natural frequencies compared to the other pore distribution patterns.

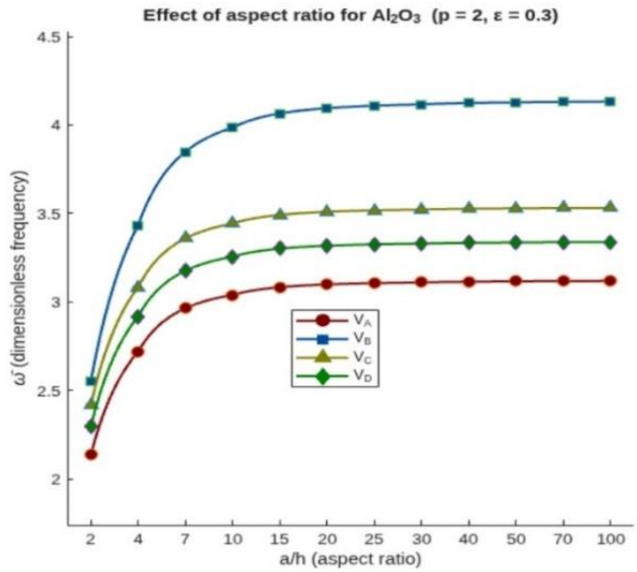

Figure 4.5 Effect of aspect ratio a/h on dimensionless frequency ω̄ for different ceramic materials (Al_2O_3, SiC, Si_3N_4) with porosity pattern C (p = 2, ε = 0.3)

The dimensionless frequency ω̄ decreases monotonically with the increase of the porosity coefficient ε, regardless of the pore distribution pattern (A, B, C, D), due to the reduction in the effective stiffness of the ceramic. Among the four patterns, pattern D (VD) exhibits the highest frequencies over the entire range of ε, indicating that it minimizes the loss of dynamic stiffness, whereas pattern A (VA) shows the most deleterious effect. This hierarchy is explained by the spatial distribution of the pores: a porosity gradient increasing toward the surface (pattern D) preserves the bending stiffness better than a uniform distribution (pattern A) or one concentrated at the core. Thus, to optimize the vibrational performance of a porous Al_2O_3 structure at a fixed aspect ratio (a/h = 10), pattern D is the most efficient.

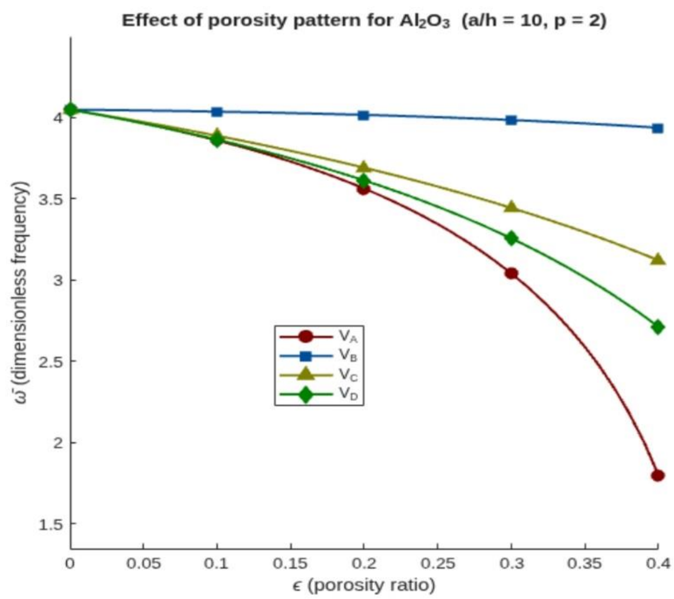

Figure 4.6 Effect of porosity ratio ε on dimensionless frequency $\bar{\omega}$ for porosity distribution patterns A, B, C, and D (Al_2O_3, a/h = 10, p = 2)

4.4 Conclusion

The validation of the analytical model shows excellent agreement with results from the literature, confirming the accuracy of the higher-order trigonometric approach. Increasing the gradient index p or the porosity coefficient ε reduces the dimensionless frequency $\bar{\omega}$ due to the loss of effective stiffness of the plates. For a low aspect ratio (a/h < 2), $\bar{\omega}$ increases rapidly with a/h, then reaches a plateau beyond a/h > 2, where the geometric effect becomes negligible. Al_2O_3 systematically exhibits the highest frequencies, followed by SiC and then Si_3N_4, due to its favorable Young's modulus-to-density ratio. Porosity pattern D (gradient toward the surface) maximizes the natural frequencies, while pattern A (uniform) shows the highest sensitivity to porosity. Finally, these results provide practical guidelines for designing lightweight and stiff porous structures tailored for harsh dynamic environments.

General Conclusion

This thesis focused on the vibration analysis of porous functionally graded material (FGM) plates subjected to severe dynamic environments. An analytical approach based on a five-variable higher-order trigonometric shear deformation theory (HSDT) was developed and coupled with Navier's solution method for simply supported boundary conditions. This formulation accurately captures the warping of transverse sections without requiring shear correction factors.

The first chapter presented the fundamental concepts of FGMs, the mechanisms of porosity formation, and the different porosity distribution laws (uniform, symmetric, and asymmetric). The second chapter compared the main plate theories, namely the Classical Plate Theory (CPT), the First-Order Shear Deformation Theory (FSDT), and the Higher-Order Shear Deformation Theory (HSDT), thereby justifying the use of a higher-order theory to accurately account for transverse shear effects in thick plates.

The detailed theoretical formulation led to a homogeneous matrix system whose solution provides the dimensionless natural frequencies. The validation results presented in Chapter 4 show excellent agreement with data available in the literature for various theories (FSDT and HSDT), confirming the robustness and accuracy of the proposed model.

The parametric study revealed several important physical trends:

- The dimensionless frequency, $\bar{\omega}$ decreases with increasing material gradient index (p) or porosity volume fraction ε, owing to the reduction in the effective stiffness of the plate.
- For low aspect ratios ($a/h < 2$), $\bar{\omega}$ increases rapidly and then reaches a plateau for ($a/h > 2$), where the influence of geometry becomes negligible.
- Al_2O_3 exhibits the highest natural frequencies, followed by SiC and Si_3N_4, due to its favorable Young's modulus-to-density ratio.
- Porosity pattern D (increasing porosity gradient toward the surface) maximizes the natural frequencies, whereas pattern A (uniform porosity distribution) exhibits the greatest sensitivity to porosity.
- These findings provide practical guidelines for the optimal design of lightweight, stiff, and porous structures subjected to vibration in aerospace, automotive, and biomedical engineering applications.

This work can be extended to other boundary conditions, coupled thermomechanical loadings, and the integration of smart materials such as piezoelectric layers for active vibration control. Furthermore, experimental validation using electron microscopy or image analysis techniques would be beneficial for refining pore distribution models and improving the predictive capability of the proposed approach.

Bibliographic reference

[1] Swaminathan, K. and Sangeetha, D.M. (2017) 'Thermal analysis of FGM plates – A critical review of various modeling techniques and solution methods', Composite Structures, 160, pp. 43-60. Doi: 10.1016/j.compstruct.2016.10.041.

[2] El-Galy, I. M., Saleh, B. I., & Ahmed, M. H. (2019). Functionally graded materials classifications and development trends from industrial point of view. SN Applied Sciences, 1, Article 1378.

[3] Wang, C.M., Reddy, J.N. and Lee, K.H. (2000) 'Theories of Plate Bending', in Shear Deformable Beams and Plates: Relationships with Classical Solutions. Amsterdam: Elsevier, pp. 89-109. Doi: 10.1016/B978-008043784-2/50006-X.

[4] Shufrin, I. and Eisenberger, M. (2022) 'Buckling of shear deformable plates subjected to nonuniform in-plane forces', in Analysis and Design of Plated Structures: Stability, 2nd edn, Vol. 1. Cambridge: Woodhead Publishing (Series in Civil and Structural Engineering), pp. 33-73. Doi: 10.1016/B978-0-12-823570-6.00010-0.

[5] Mohammadi, M., Rajabi, M., & Ghadiri, M. (2021). Functionally graded materials (FGMs): A review of classifications, fabrication methods and their applications. Processing and Application of Ceramics, 15(4), 319–343.

[6] Ansari, M. I., Kumar, A., Barnat-Hunek, D., Suchorab, Z., & Kwiatkowski, B. (2019). Investigation of porosity effect on flexural analysis of doubly curved FGM conoids. Science and Engineering of Composite Materials, 26(1), 435–450.

[7] S. Merdaci, H. M. Adda, B. Hakima, R. Dimitri, and F. Tornabene, "Higher-order free vibration analysis of porous functionally graded plates," J. Compos. Sci., vol. 5, no. 11, p. 305, Nov. 2021, doi: 10.3390/jcs5110305.

[8] Ton-That, H. L. (2020). The linear and nonlinear bending analyses of functionally graded carbon nanotube-reinforced composite plates based on the novel four-node quadrilateral element. European Journal of Computational Mechanics, 29(1), 139–172.

[9] Mittelstedt, C. (2025). Higher-order laminate theories. In Mechanics of composite structures (pp. 299–366). Springer. https://doi.org/10.1007/978-3-662-70788-3_11

[10] El-Hadad, S., Sato, H., Miura-Fujiwara, E., & Watanabe, Y. (2010). Fabrication of Al-Al3Ti/Ti3Al functionally graded materials under a centrifugal force. Materials, 3(9), 4639–4656.

[11] Van Long, N., Minh Tu, T., Quy Truong, H., Thanh Hai, L., & Thi Thu Trang, V. (2022). Displacement-based and stress-based analytical approaches for nonlinear bending analysis of functionally graded porous plates resting on elastic substrate. Acta Mechanica, 233(6), 1689–1714.

[12] Malha, N., Tiberkak, R., Ezzraimi, M., Lazar, M. E., & Attaf, B. (2024). Active vibration control of functionally graded material plates integrated with piezoelectric layers using new Q9γ approach. Journal of Mechanics, 40, 95–111.

[13] Shi, H., Zhou, P., Li, J., Liu, C., & Wang, L. (2021). Functional gradient metallic biomaterials: Techniques, current scenery, and future prospects in the biomedical field. Frontiers in Bioengineering and Biotechnology, 8, Article 616845.

[14] Singh, J., Kumar, A., Szafraniec, M., Barnat-Hunek, D., & Sadowska-Buraczewska, B. (2022). Static analysis of skew functionally graded plate using novel shear deformation theory. Materials, 15(13), Article 4633.

[15] Bohidar, S. K., Sharma, R., & Mishra, P. R. (2014). Functionally graded materials: A critical review. International Journal of Research, 1(7), 289–301.

[16] Abbasgholipourghadim, M., Mailah, M. B., Zaurah, I., Ismail, A. F., & Rezaei Dashtarzh, M. (2016). Membrane surface porosity and pore area distribution incorporating digital image processing. International Journal of Mechanics, 10, 124–131.

[17] A., Olawuyi, B. J., Boshoff, W. P., & le Roux, S. G. (2016). Simple and fast porosity analysis of concrete using X-ray computed tomography. Materials and Structures, 49, 553–562.

[18] Cho, J. R., & Oden, J. T. (2000). Functionally graded material: a parametric study on thermal-stress characteristics using the Crank-Nicolson-Galerkin scheme. Computer Methods in Applied Mechanics and Engineering, 188(1-3), 17–38.

[19] Vrabie, M., & Băetu, S. (2013). Comparative analysis of the bending theories for isotropic plates. Case study. Buletinul Institutului Politehnic din Iaşi, Secţia Construcţii. Arhitectură, Tomul LIX (LXIII), Fasc. 3.

[20] Singh, J., Kumar, A., Szafraniec, M., Barnat-Hunek, D., & Sadowska-Buraczewska, B. (2022). Static Analysis of Skew Functionally Graded Plate Using Novel Shear Deformation Theory. Materials, 15(13), 4633.

[21] Shinohara, Y. (2013) ‘Functionally Graded Materials’, in Handbook of Advanced Ceramics: Materials, Applications, Processing, and Properties. 2nd edn. Amsterdam: Elsevier, pp. 1179-1187. Doi: 10.1016/B978-0-12-385469-8.00061-7.

[22] Yamanouchi, M., Koizumi, M., Hirai, T., & Shiota, I. (Eds.). (1990). Proceedings of the First International Symposium on Functionally Gradient Materials. Functionally Gradient Materials Forum. Sendai, Japan, October 8-9, 1990.

[23] Koizumi, M. (1993). "The concept of FGM." Ceramic Transactions: Functionally Graded Materials, Vol. 34, pp. 3-10. The American Ceramic Society, Westerville, Ohio.